J. Fluid Mech. (2021), *vol.* 920, A22, doi:10.1017/jfm.2021.450

JFM PAPERS

Time domain modelling of a Helmholtz resonator analogue for water waves

Leo-Paul Euvé[1,2,†], **Kim Pham**[3], **Philippe Petitjeans**[1], **Vincent Pagneux**[4] **and Agnès Maurel**[5]

[1]PMMH, ESPCI, Sorbonne Université, Université PSL, 1 rue Jussieu, 75005 Paris, France

[2]Bluerium, Av. L. Philibert, 13100 Aix-en-Provence, France

[3]IMSIA, CNRS, EDF, CEA, ENSTA Paris, Institut Polytechnique de Paris, 828 Bd des Maréchaux, 91732 Palaiseau, France

[4]Lab. d'Acoustique de l'Université du Mans (LAUM), Av. O. Messiaen, 72085 Le Mans

[5]Institut Langevin, ESPCI Paris, Université PSL, CNRS, 1 rue Jussieu, 75005 Paris, France

(Received 6 January 2021; revised 13 May 2021; accepted 15 May 2021)

In the context of water waves, we consider a resonator with deep subwavelength resonance, analogue to the Helmholtz resonator in acoustics. In the shallow water regime, using asymptotic analysis, a one-dimensional model is derived in which the effect of the resonator is reduced to effective transmission conditions. These conditions clearly highlight two contributions. The first is associated with the dock on its own and it is responsible for a jump of the potential at the free surface. The second is due to the resonant cavity and it is responsible for a jump in the horizontal velocity. It involves as well the uniform amplitude within the resonant cavity with a transient dynamics explicitly given by the equation of a damped oscillator forced by the incident waves. The one-dimensional model is validated in the harmonic regime by comparison to direct two-dimensional numerics. It is shown to reproduce accurately the scattering coefficients and the amplitude within the resonator; interestingly, this remains broadly true for finite water depths. We further inspect the spatio-temporal behaviour of different types of wave packets interacting with the resonating and radiating cavity.

Key words: surface gravity waves, wave scattering

1. Introduction

The modern design of devices able to control the energy flow of water waves has begun to benefit from the development of metamaterials. For instance, the propagation can be made anisotropic using varying bathymetry, see e.g. Maurel *et al.* (2017), Maurel, Pham & Marigo (2019) and Porter (2019), or it can be guided due to valley-locked

---

† Email address for correspondence: leo-paul.euve@espci.fr

transport (Makwana *et al.* 2020). In addition, a plethora of interesting phenomena has been proposed, such as the cancellation of the scattering by rigid obstacles and their cloaking (Newman 2014; Dupont *et al.* 2016; Porter 2018; Bobinski *et al.* 2018; Iida & Kashiwagi 2018; Farhat *et al.* 2020), the perfect absorption of the wave energy in the nonlinear regime (Monsalve *et al.* 2019) and the trapping for energy harvesting using graded arrays of resonators (Bennetts, Peter & Craster 2018, 2019).

Apart from Bragg type resonances due to a periodic bathymetry (Mei, Stiassnie & Yue 1989; Porter & Porter 2003) or due to the interaction of several rigid obstacles within an array (Linton 2011; Archer *et al.* 2020), strategies using local resonances of a single resonator have been developed. In most of the cases, vertically invariant resonators have been envisioned (Dupont *et al.* 2017; Monsalve *et al.* 2019; Bennetts *et al.* 2018, 2019). This means that the wave dynamics modelling can use separation of variables between vertical and horizontal coordinates resulting in a Helmholtz equation at the free surface identical to the two-dimensional acoustic case. In the present study we consider a different type of local resonance inspired by acoustic Helmholtz resonators (HRs). These resonators are cavities or bottles connected to the surrounding air by a thin neck which are used to produce sound waves of specific tones with resonance wavelengths much smaller than the dimensions of the bottle (Ingard 1953; Helmholtz & Ellis 1954). Such subwavelength resonances are made possible as the cavity is almost closed, allowing for an almost zero-frequency mode as the radiative damping is weak. We envisage that such a resonator for water waves would be made possible using an underwater cavity. The main difference between an acoustic HR and the water-wave resonator that we propose is that the former is governed by the Helmholtz equation while the latter is governed by the Laplace equation. Next, the compressibility in the acoustic cavity is replaced by the restoring force at the free surface of the water-wave cavity, allowing for the resonance to take place. Interestingly the water-wave HRs exist for both two- and three-dimensional water waves while the acoustic HR previously mentioned exists only for three-dimensional water waves with vertically invariant obstacles, see e.g. Monsalve *et al.* (2019). In the present study, we shall consider the water-wave HRs in two dimensions.

The geometry, sketched in figure 1, consists of a cavity fixed on the free surface and coupled to the sea thanks to a thin neck on its bottom. In the absence of the neck ($L_o \rightarrow \ell$), this geometry degenerates to the famous oscillating water column (OWC). OWC devices have received attention since the pioneering work of Isaacs & Wiegel (1949) who were interested in using open-end pipes with float-type recorders for measuring wave heights. In the 1970s, it was identified as the first resonator able to produce zero transmission resonances in the context of water waves (Evans & Morris 1972; Newman 1974; Evans 1975, 1978). We can notice that compressed air breakwaters related to OWC have been also envisioned (Linton & Evans 1990). More recently, studies have been conducted on vertical openings through ship hulls, called moonpools (Molin 2001; Ravinthrakumar *et al.* 2019), and gaps in between two ships side by side in offloading operations (Molin *et al.* 2018; Zhao *et al.* 2020). In these configurations, the lowest resonance corresponds to a piston mode associated with a velocity potential varying linearly along the vertical direction in the device, be it the gap or the moonpool. As such, the resonance frequency is governed by the immersion depth of the cavity resulting in a resonance of the quarter-wavelength type modified by the dynamical condition at the free surface. In contrast, our HR resonance is associated with a constant potential within the cavity whose resonance frequency, for given dimensions of the cavity, can be reduced to arbitrarily low value in the lossless case. Consequently, and importantly, the resonator we present here opens possibilities to tend to a very subwavelength regime.

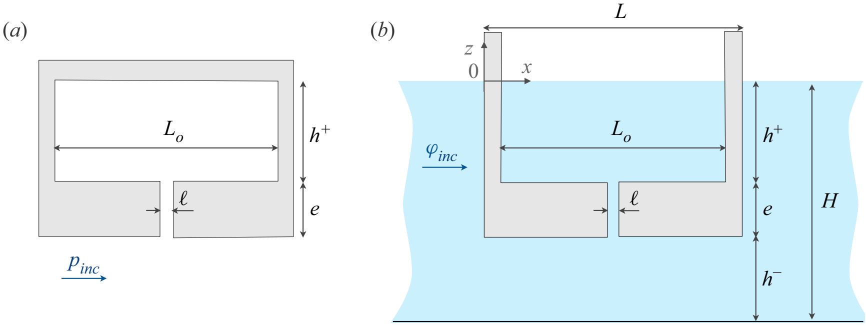

Figure 1. (*a*) A HR for acoustic waves composed of a resonant cavity of dimension L_o, h^+ and a long thin neck of dimensions e, ℓ. (*b*) The analogue resonator for water waves, with the dynamic boundary condition at the free surface playing the role of the acoustic compressibility.

To get a basic understanding of the resonance mechanism, and before going into more sophisticated analysis, let us first inspect heuristically the analogy between the acoustic HR and water-wave HR sketched in figure 1. Although we shall derive later a model in the shallow water regime, we stress that the analogy between acoustic and water-wave HRs applies more generally since the dynamic boundary condition at the free surface for the water waves plays the role of the compressibility in acoustics. In the context of acoustic waves, the acoustic pressure p and velocity $\boldsymbol{u}$ are governed by the linearized Euler equations, $\rho \partial_t \boldsymbol{u} = -\nabla p$, $\beta \partial_t p + \operatorname{div} \boldsymbol{u} = 0$, with ρ the mass density and β the non-vanishing compressibility of the fluid. The resonance frequency is obtained by integrating the equation of mass conservation over the domain $\varOmega$ of the cavity where the pressure p_R is uniform. Assuming in addition that the vertical velocity $v_{|N}$ in the neck is constant (hence $\rho \partial_t v_{|N} = -1/e(p_R - p_{|N})$) we obtain the sequence of equations

$$\left\{\begin{aligned} &\int_{\varOmega} (\operatorname{div} \boldsymbol{u} + \beta \partial_t p)\,\mathrm{d}\boldsymbol{x} = 0, \quad \longrightarrow \quad \beta (L_o h^+) \partial_t p_R - \ell\, v_{|N} = 0, \\ &\partial_{tt} p_R + \omega_0^2 p_R = \omega_0^2 p_{|N}, \quad \omega_0 = c\sqrt{\frac{\ell}{e L_o h^+}}, \end{aligned}\right. \tag{1.1}$$

with $c = \sqrt{1/(\rho\beta)}$ the speed of sound. At this stage the pressure $p_{|N}$ at the bottom end of the neck is unknown but the resonance frequency ω_0 has been determined. In the context of water waves, the fluid is incompressible but the dynamic boundary condition at the free surface $v = -(1/g)\,\partial_{tt}\varphi$ provides a spring contribution analogue to that of the compressibility in acoustic (v denotes the vertical velocity, φ the potential and g the gravity constant). Assuming as previously that the potential φ_R is uniform in the cavity and that the velocity is constant in the neck (hence $v_{|N} = 1/e(\varphi_R - \varphi_{|N})$), we integrate $\operatorname{div} \boldsymbol{u} = 0$ over the domain of the cavity to get

$$\left\{\begin{aligned} &\int_{\varOmega} \operatorname{div} \boldsymbol{u}\,\mathrm{d}\boldsymbol{x} = 0, \quad \longrightarrow \quad -\frac{L_o}{g} \partial_{tt} \varphi_R - \ell\, v_{|N} = 0, \\ &\partial_{tt} \varphi_R + \omega_0^2 \varphi_R = \omega_0^2 \varphi_{|N}, \quad \omega_0 = \sqrt{\frac{g\ell}{e L_o}}. \end{aligned}\right. \tag{1.2}$$

As in the acoustic case, the potential $\varphi|_N$ at the bottom end of the neck is unknown but the resonance frequency has been determined. The resonance in (1.2) is the analogue of that in (1.1) and the analogy is perfect in the shallow water regime with $c = \sqrt{gh^+}$ within the cavity.

In the following , we use asymptotic analysis to go beyond the previous heuristic analysis and we derive a time domain model coupling the resonator with the surrounding water dynamics. This is done using asymptotic analysis thanks to a small parameter measuring the dimension of the cavity normalized to the typical wavelength. In the shallow water regime, with a water depth to cavity immersion of the order of unity, the problem is reduced to the classical shallow water equation outside the resonator. Besides, since the resonator has subwavelength dimensions, its effect is asymptotically encoded in effective transmission conditions. These conditions tell us that the potential and the horizontal velocity are discontinuous across the resonator. The discontinuity of the potential is related to the dock problem ($\ell = 0$) while that of the horizontal velocity is related to the resonance. The latter involves the uniform potential $\varphi_R(t)$ in the cavity governed by the equation of a forced damped oscillator, see forthcoming equation (2.11). The damping is radiative and due to the coupling of the cavity with the surrounding water; without surprise, the forcing term is the incident wave. The model is presented in § 2 and its solution is obtained in the transient regime; to highlight the obtained results, the technicalities of the asymptotic expansions are collected in Appendix B. In § 3, the asymptotic model is validated in the harmonic regime by comparison to direct numerics based on modal method, and its validity for finite water depths is inspected. It is stressed that the asymptotic solution provides a comprehensive picture of the resonant dynamics although it introduces errors in the resonant frequency. In § 4 different types of incident wave packets are considered, revealing the capacity of the resonator to radiate waves over long times, being weakly coupled to the surrounding water.

2. The actual problem and the reduced problem – summary of the main result

2.1. *The actual problem*

Using the assumptions of an inviscid, incompressible fluid, and an irrotational motion, the linearized equation for the velocity potential $\phi(\boldsymbol{r}, t)$ reads

$$\begin{cases} \Delta\phi = 0, \\ \partial_z\phi_{|z=0} = -\dfrac{1}{g}\,\partial_{tt}\phi_{|z=0}, \quad \nabla\phi\boldsymbol{\cdot}\boldsymbol{n}_{|\Gamma} = 0, \end{cases} \tag{2.1}$$

where t is the time, $\boldsymbol{r} = (x, z)$ with x the horizontal coordinate and z the vertical one (Mei, Stiassnie & Yue 2005). Next, $z = 0$ is the undisturbed free surface, $z = -H$ the sea bottom and Γ denotes the boundaries of the rigid parts of the resonator and of the sea bottom. Eventually, the free surface elevation $\eta(x, t)$ and velocity $\boldsymbol{u} = (u, v)$ are defined by

$$\boldsymbol{u}(\boldsymbol{x}, t) = \nabla\phi(\boldsymbol{x}, t), \quad \eta(x, t) = -\frac{1}{g}\partial_t\varphi(x, t), \tag{2.2a,b}$$

where $\varphi(x, t) = \phi(x, 0, t)$ is the potential at the free surface.

2.2. *The reduced problem*

In the time domain, the shallow water regime requires that the maximum frequency ω imposed by the source satisfies $\omega^2 H/g \ll 1$, and with the exception of § 3.2, we restrict our study to this case. Assuming in addition that L is of the same order of magnitude as H and that the neck opening ℓ is much smaller than all the other dimensions of the resonator,

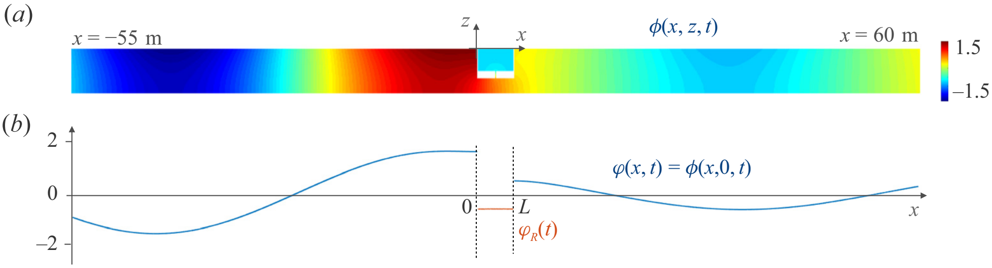

Figure 2. Meaning of the reduction of model. (*a*) The solution of the actual problem is computed numerically on the velocity potential $\phi(x, z, t)$ solution of (2.1). (*b*) The solution of the reduced problem is computed for $\varphi(x, t) = \phi(x, 0, t)$ for $x \notin (0, L)$ solution of (2.3) and $\varphi_R(t) = \phi(x, 0, t)$ for $x \in (0, L)$ solution of (2.11) for an incident wave $\varphi_{inc}(x, t)$.

the actual problem can be reduced to a one-dimensional problem along x which applies for the velocity potential at the free surface $\varphi(x, t)$ (figure 2). Specifically, the reduced problem whose derivation is detailed in Appendix B reads

$$\begin{cases} gH\,\partial_{xx}\varphi(x,t) - \partial_{tt}\varphi(x,t) = 0, \quad x \in (-\infty, 0) \cup (L, +\infty), \\ \llbracket \varphi \rrbracket(t) = H\mathcal{B}\,\overline{\partial_x\varphi}(t), \quad \llbracket \partial_x\varphi \rrbracket(t) = \dfrac{L_o}{gH}\,\ddot{\varphi}_R(t), \quad \ddot{\varphi}_R(t) + \omega_0^2\varphi_R(t) = \omega_0^2\,\bar{\varphi}(t), \end{cases} \tag{2.3}$$

where $\llbracket \varphi \rrbracket(t) = \varphi(L, t) - \varphi(0, t)$ is the jump of φ across the resonator and $\overline{\varphi} = (\varphi(0, t) + \varphi(L, t))/2$ the mean value (the same for $\llbracket \partial_x\varphi \rrbracket$ and $\overline{\partial_x\varphi}$), $\varphi_R(t)$ is the uniform potential in the cavity (dot stands for the time derivative). At it should be, the surrounding fluid satisfies the shallow water equation for a constant water depth H.

The effect of the resonator has been encapsulated in effective transmission conditions which constitute the main results of the present analysis. The first condition on the jump of the potential $\llbracket \varphi \rrbracket$ across the resonator (between $x = 0$ and $x = L$) involves the mean value of the horizontal velocity. It is the condition obtained for a dock on its own. In this context, $\mathcal{B}$ is the blockage coefficient appearing in the problem of a perfect fluid flowing in a rigid duct containing a constriction having the form of the dock (Bartholomeusz 1958; Tuck 1975, see also Appendix A). The second condition links the jump of the horizontal velocity $\llbracket \partial_x\varphi \rrbracket$ across the resonator to the second time derivative $\ddot{\varphi}_R(t)$ of $\varphi_R(t)$ which is the uniform velocity potential within the resonant cavity. Eventually, apart from the geometrical parameters, the model (2.3)–(2.11) involves a blockage coefficient $\mathcal{B}$ and a so-called effective length e_{eff}. The former has an explicit expression and the latter can be evaluated (see Appendix A); they read

$$\begin{cases} \mathcal{B} = \dfrac{L}{h^-} + 2\mathcal{B}_\mu, & \mu = \dfrac{h^-}{H}, \\ e_{eff} = e + \dfrac{\ell}{2}\left(\mathcal{B}_\mu + \mathcal{B}_{\mu_0}\right), & \mu = \dfrac{\ell}{L}, \mu_0 = \dfrac{\ell}{L_o}, \end{cases} \tag{2.4}$$

where $\mathcal{B}_\mu$ is a function of μ only, defined by

$$\mathcal{B}_\mu = \frac{1}{\pi}\frac{(\mu^2+1)}{\mu}\log\frac{1+\mu}{1-\mu} - \frac{2}{\pi}\log\frac{4\mu}{1-\mu^2}. \tag{2.5}$$

2.3. *D'Alembert formulation of the solutions*

In the presence of a right-going incident wave φ_{inc}, the reduced problem (2.3) can be solved explicitly using d'Alembert solutions (d'Alembert 1747). Specifically, we use that the solution can be written, denoting $c = \sqrt{gH}$, as

$$\varphi(x,t) = \begin{cases} \varphi_{inc}(t - x/c) + \varphi^{-}(t + x/c), & x \in (-\infty, 0), \\ \varphi^{+}(t - (x - L)/c), & x \in (L, +\infty), \end{cases} \tag{2.6}$$

where φ^{+} is the transmitted right-going wave and φ^{-} is the reflected left-going wave. From (2.6) we have $[\![\varphi]\!] = \varphi^{+}(t) - \varphi^{-}(t) - \varphi_{inc}(t)$, $\overline{\partial_x \varphi} = -1/2c(\dot\varphi^{+}(t) - \dot\varphi^{-}(t) + \dot\varphi_{inc}(t))$ and $[\![\partial_x\varphi]\!] = -1/c(\dot\varphi^{+}(t) + \dot\varphi^{-}(t) - \dot\varphi_{inc}(t))$. Reporting these expressions in the transmission conditions (2.3) we obtain that $\varphi_{dock} = (\varphi^{+} - \varphi^{-} - \varphi_{inc})/2$ and $\varphi_{res} = (\varphi^{+} + \varphi^{-} - \varphi_{inc})/2$ satisfy

$$\dot\varphi_{res}(t) = -\frac{2}{\omega_0^2\tau}\ddot\varphi_R(t), \quad \dot\varphi_{dock}(t) + \frac{1}{\tau_{dock}}\varphi_{dock}(t) = -\dot\varphi_{inc}(t), \tag{2.7a,b}$$

where

$$\tau_{dock} = \frac{\mathcal{B}}{2}\sqrt{\frac{H}{g}}, \tag{2.8}$$

and where we have used that $cL_o/gH = 4/\omega_0^2\tau$. Eventually, the waves emitted by the resonator are given by

$$\varphi^{-}(t) = \varphi_{res}(t) - \varphi_{dock}(t), \quad (\varphi^{+}(t) - \varphi_{inc}(t)) = \varphi_{res}(t) + \varphi_{dock}(t), \tag{2.9a,b}$$

from which we deduce that

$$\bar\varphi(t) = \varphi_{inc}(t) - \frac{2}{\omega_0^2\tau}\dot\varphi_R(t). \tag{2.10}$$

Hence, the harmonic oscillator equation in (2.3) that governs the potential φ_R inside the cavity takes the form

$$\begin{cases} \ddot\varphi_R(t) + \dfrac{2}{\tau}\dot\varphi_R(t) + \omega_0^2\varphi_R(t) = \omega_0^2\,\varphi_{inc}(t), \\ \text{where } \omega_0 = \sqrt{\dfrac{g\ell}{e_{\mathit{eff}}L_o}}, \quad \tau = \dfrac{4e_{\mathit{eff}}}{\ell}\sqrt{\dfrac{H}{g}}, \end{cases} \tag{2.11}$$

which corresponds to the equation of a damped resonator, with ω_0 the resonance frequency and τ the characteristic time of the radiative damping due to the coupling of the resonator with the surrounding fluid. Eventually, $\varphi_{inc}(t - x/c) = \phi_{inc}(x, 0, t)$ is the potential associated with the incident wave at the free surface.

The above general solution confirms the kind of contributions of the resonator and of the dock that were already visible from the transmission conditions in (2.3): the resonator acts as a monopole radiating $\varphi_{res}(t)$ symmetrically toward $x < 0$ and $x > L$; the dock on its own acts as a dipole radiating $\pm\varphi_{dock}(t)$ toward $x < 0$ and $x > L$. Incidentally, we also obtain that $\bar{\varphi}(t) = \varphi_{inc}(t) + \varphi_{res}(t)$, which provides (2.10) using (2.7*a*,*b*). Eventually, with ℓ much smaller than the other dimensions of the problem, we have

$$\omega_0\tau = 4\sqrt{\frac{eH}{L_o\ell}} \gg 1, \quad \omega_0\tau_{dock} = \frac{\mathcal{B}}{2}\sqrt{\frac{H\ell}{eL_o}} \ll 1. \tag{2.12a,b}$$

The first relation tells us that, because of its thin neck, the resonator is weakly coupled to the surrounding water. In contrast, the response of the dock up to the resonance frequency (at least) is dictated by the incident wave, as $\varphi_{dock}(t) \sim -\tau_{dock}\dot{\varphi}_{inc}(t)$.

3. Validation of the reduced problem in the harmonic regime

We start by analysing the reduced problem in the harmonic regime, in order to easily validate the reduced model by comparison to direct numerics. The numerics uses a classical multimodal method to compute the solution of the actual problem (2.1); the method is detailed in Appendix C.

The results presented in this section are obtained for the following geometry: $H = 6$ m, $L = 5$ m, $L_o = 4.8$ m, $e = 1$ m, $\ell = 0.1$ m, $h^- = 2$ m ($h^+ = 3$ m) and we consider the frequency range $\omega \in (0, 1)$ rad s^{-1}. The resulting parameters are: $\tau_{dock} = 1.35$ s, $\omega_0 = 0.40$ rad s^{-1} and $\tau = 38.3$ s. (with $\mathcal{B} = 3.45$ and $e_{eff} = 1.22$ m).

3.1. *Solution in the harmonic regime*

In the harmonic regime at frequency ω, we denote $\varphi(x, t) = \mathrm{Re}(\tilde{\varphi}(x, \omega)\mathrm{e}^{-\mathrm{i}\omega t})$ and we consider an incident wave with unitary amplitude $\tilde{\varphi}_{inc}(x, \omega) = \mathrm{e}^{\mathrm{i}kx}$, where $k = \omega/\sqrt{gH}$ is the wavenumber in $x \in (-\infty, 0) \cup (L, +\infty)$. The complex uniform potential $\tilde{\varphi}_R(\omega)$ in the cavity solution to (2.11) and the potentials $\tilde{\varphi}_{dock}(\omega)$ and $\tilde{\varphi}_{res}(\omega)$ solutions to (2.7*a*,*b*), read

$$\left\{\begin{aligned} &\tilde{\varphi}_R(\omega) = \frac{\omega_0^2}{\left(\omega_0^2 - \omega^2 - \dfrac{2\mathrm{i}\omega}{\tau}\right)}, \\ &\tilde{\varphi}_{dock}(\omega) = \frac{\mathrm{i}\omega\tau_{dock}}{(1 - \mathrm{i}\omega\tau_{dock})}, \quad \tilde{\varphi}_{res}(\omega) = \frac{\dfrac{2\mathrm{i}\omega}{\tau}}{\left(\omega_0^2 - \omega^2 - \dfrac{2\mathrm{i}\omega}{\tau}\right)}. \end{aligned}\right. \tag{3.1}$$

Introducing the scattering coefficients (R, T) for the potential $\tilde{\varphi}$ in the form

$$\tilde{\varphi}(x < 0, \omega) = \left(\mathrm{e}^{\mathrm{i}kx} + R(\omega)\mathrm{e}^{-\mathrm{i}kx}\right), \quad \tilde{\varphi}(x > L, \omega) = T(\omega)\mathrm{e}^{\mathrm{i}k(x-L)}, \tag{3.2a,b}$$

and identifying with (2.6)–(2.9*a*,*b*) we obtain $\tilde{\varphi}^-(\omega) = R(\omega)$ and $\tilde{\varphi}^+(\omega) = T(\omega)$, hence

$$\left\{\begin{aligned} &R = \frac{1}{2}\frac{\left(\omega_0^2 - \omega^2 + \dfrac{2\mathrm{i}\omega}{\tau}\right)}{\left(\omega_0^2 - \omega^2 - \dfrac{2\mathrm{i}\omega}{\tau}\right)} - \frac{1}{2}\frac{(1 + \mathrm{i}\omega\tau_{dock})}{(1 - \mathrm{i}\omega\tau_{dock})}, \\ &T = \frac{1}{2}\frac{\left(\omega_0^2 - \omega^2 + \dfrac{2\mathrm{i}\omega}{\tau}\right)}{\left(\omega_0^2 - \omega^2 - \dfrac{2\mathrm{i}\omega}{\tau}\right)} + \frac{1}{2}\frac{(1 + \mathrm{i}\omega\tau_{dock})}{(1 - \mathrm{i}\omega\tau_{dock})}, \end{aligned}\right. \tag{3.3}$$

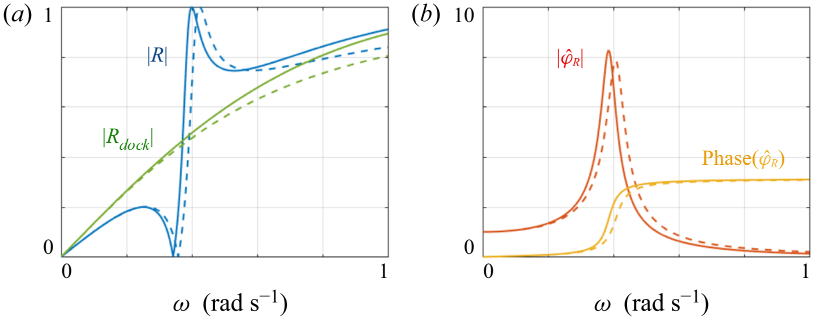

Figure 3. Validation of the reduced model solution (dashed lines) by comparison to direct numerical calculations (plain lines). (*a*) Reflection coefficient $|R(\omega)|$ against $\omega \in (0, 1)$ rad s^{-1}; for comparison, $|R_{dock}|$ for a dock on its own ($\ell = 0$) is reported. In the reduced model, we use (3.3)–(3.4*a*,*b*). (*b*) Velocity potential $\tilde{\varphi}_R(\omega)$ (magnitude and phase) within the resonator. In the reduced model we use (3.1).

which satisfy $|R|^2 + |T|^2 = 1$. For the dock on its own, $\varphi_R = 0$, resulting in

$$R_{dock} = \frac{1}{2} - \frac{1}{2}\frac{(1 + \mathrm{i}\omega\tau_{dock})}{(1 - \mathrm{i}\omega\tau_{dock})}, \quad T_{dock} = 1 - R_{dock}. \tag{3.4a,b}$$

Eventually, the amplitude within the cavity given by (3.1) reaches a maximum at the resonance with

$$\tilde{\varphi}_R(\omega_0) = \frac{\mathrm{i}\omega_0\tau}{2} = 2\mathrm{i}\sqrt{\frac{e_{eff}H}{\ell L_o}}. \tag{3.5}$$

We have calculated numerically the solution of the actual problem (2.1) for $\omega \in (0, 1)$ rad s^{-1}. We report in figure 3 the variations of $|R(\omega)|$ and $\tilde{\varphi}_R(\omega)$. In panel (*a*), we see that the resonance curve $|R(\omega)|$ has a highly asymmetric profile characteristic of a Fano resonance, with sharp variations producing perfect and zero reflection. We also report the underlying smooth curve corresponding to the background scattering of the dock on its own. In the context of water waves, similar variations have been reported in Parsons & Martin (1994) due to Mie resonances occurring when a submerged obstacle rises to the free surface. Panel (*b*) shows the corresponding amplitude within the cavity with rapid variations in magnitude and phase (from 0 to π). It is worth noticing that the resonance is deeply subwavelength with an incident wavelength $\lambda = 2\pi\sqrt{gH}/\omega_0$ 30 times larger than the dimensions, L and h^+, of the resonator. The predictions of the reduced model, R in (3.3), R_{dock} in (3.4*a*,*b*) and $\tilde{\varphi}_R$ in (3.1), are in good agreement with the direct numerics with two distinct sources of discrepancy. On the one hand, in the vicinity of the resonance, we observe a systematic shift of around 0.02 rad s^{-1} between the resonance curve calculated numerically and the theoretical one. Specifically, the model predicts a resonance frequency $\omega_0 = 0.41$ rad s^{-1} from (2.11) and a succession of a perfect reflection at ω_1 and a perfect transmission at ω_2 given, from (3.3), by

$$\omega_1 = \sqrt{\omega_0^2 - 2(\tau\tau_{dock})^{-1}}, \quad \omega_2 = \frac{\omega_0}{\sqrt{1 - 2\tau_{dock}\tau^{-1}}}, \tag{3.6a,b}$$

(in the present case, $\omega_1 = 0.36$ rad s^{-1} and $\omega_2 = 0.42$ rad s^{-1}) while the actual, numerical values are lower; this is attributable to the approximate added length which could be refined by conducting the analysis at higher order. On the other hand, the scattering strength of the dock on its own, measured here by $|R_{dock}|$, is underestimated by the model

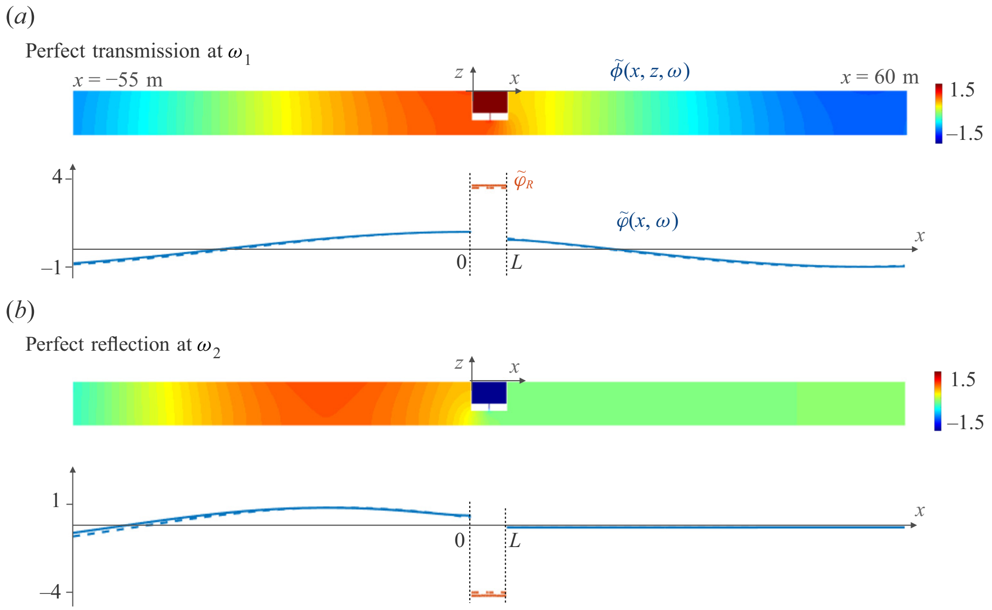

Figure 4. Two-dimensional fields $\tilde{\phi}(x, z, \omega)$ and corresponding profiles $\tilde{\varphi}(x, \omega)$ at the free surface at $\omega = \omega_1$ (perfect transmission) and ω_2 (perfect reflection). The profiles show $\tilde{\varphi}(x, \omega)$ outside the resonator (blue lines) and $\tilde{\varphi}_R(\omega)$ inside the cavity (red lines). The plain lines show the numerical results and the dashed lines the results of the model (3.2*a*,*b*)–(3.3).

above 0.4 rad s^{-1} ($kH \simeq 0.3$) as the assumption of the shallow water regime becomes less valid. As expected, the shift in the resonance frequency is recovered in the resonant curve $\tilde{\varphi}_R(\omega)$. However, the model reproduces correctly that the amplitude within the cavity is the same as outside for long waves ($\omega \rightarrow 0$) while it tends to zero for shorter waves. Indeed for these latter, the cavity behaves as a closed cavity.

The two-dimensional fields $\tilde{\phi}(x, z, \omega)$ computed numerically at the frequencies ω_1 and ω_2 are shown in figure 4. In both cases, the large amplitude within the cavity is constant although a zoom reveals strong contributions of the evanescent field excited at the ends of the neck (not shown) that are taken into account by added lengths. With $\omega_1 < \omega_0 < \omega_2$, and according to the phase variations in figure 3, the perfect transmission corresponds to an oscillation within the cavity in phase with the incident wave at $x = 0$. Conversely, the perfect reflection corresponds to an oscillation within the cavity oscillating in phase quadrature with the incident wave at $x = 0$. This is also visible from (3.1), along with (2.12*a*,*b*) and (3.6*a*,*b*). Accounting for the small shift in the reflection curves between the numerics and the model, we also report the profiles of the potential at the free surface outside and inside the cavity. Again, the agreement is good, in particular the constant shape of $\tilde{\varphi}_R$ in the cavity is confirmed.

3.2. *From the shallow to the deep water-wave regime*

Our analysis has been conducted in the shallow water regime which allows us to obtain a one-dimensional reduced model. However, most of the asymptotic analysis is done in the vicinity of the resonator independently of the water depth (see Appendix B). Thus, it makes sense to inspect whether or not the model remains predictive when we move from the shallow water regime to the finite depth regime. We have computed numerically the

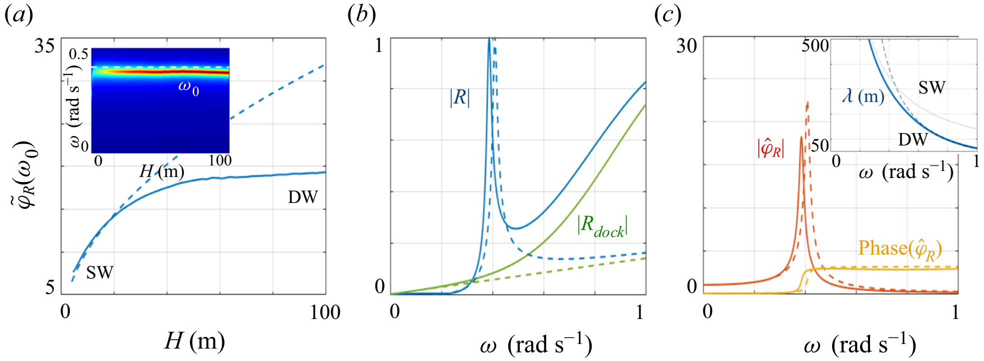

Figure 5. From shallow (SW) to deep water (DW). (*a*) Variations of $\tilde{\varphi}_R(\omega_0)$ against H, calculated numerically (plain line) and from (3.5) (dashed lines). The inset shows $\tilde{\varphi}_R$ in colour scale against ω and H calculated numerically; the dashed white line shows $\omega = \omega_0$ from (2.3). (*b*,*c*) Show $|R(\omega)|$ and $\tilde{\varphi}_R(\omega)$ for $H = 50$ m, same representation as in figure 3. The inset in panel (*c*) shows $\lambda(\omega)$ moving from the SW to the DW regime.

potential $\tilde{\varphi}_R(\omega)$ for various $H \in (4, 100)$ m. The result is shown in the inset of figure 5(*a*). We observe that the frequency ω_0 realizing the maximum is independent of H and it agrees with (2.3). This confirms that the resonance frequency is characteristic of the resonator on its own. Next, the resonant amplitude $|\tilde{\varphi}_R(\omega_0)|$ increases with H for small H in agreement with (3.5), afterwards, it saturates (above $H \simeq 40$ m in the main plot in (*a*)). In the shallow water regime, the increase of the resonant amplitude with H tells us that the presence of the sea bottom below the cavity weakens the resonance; a similar confinement effect has been reported for acoustic HRs (Maurel *et al.* 2019). However, as the water depth increases, this effect vanishes and the amplitude tends to a value corresponding to the resonance in the deep water regime (hence, independent of H).

Panels (*b*,*c*) show $|R(\omega)|$ and $\tilde{\varphi}_R(\omega)$ for the intermediate water depth $H = 50$ m. The shape of the resonance curve differs significantly from that reported in the shallow water regime in figure 3. The main reason is that the scattering strength of the dock on its own is weak around the resonance. As in figure 3, we report for comparison the predictions for $\tilde{\varphi}_R$ from (3.1), R from (3.3) and R_{dock} from (3.4*a*,*b*). The most noticeable error in the reduced model is already visible on R_{dock} which is underestimated for $\omega > 0.2$ rad s^{-1}. The same occurs for R as R tends to R_{dock} outside the resonance. The shallow water approximation used in the model overestimates the wavelength, hence it erroneously predicts that the wave can pass easily through the dock. In the reported case, the reflection is significant, up to 4 times the value predicted by the shallow water approximation (at $\omega = 1$ rad s^{-1}). In contrast, the overall variations of the amplitude $\tilde{\varphi}_R$ in the cavity are well reproduced by the reduced model (we know from (*a*) that the maximum is overestimated). Below the resonance, the cavity behaves as an open cavity, $|\tilde{\varphi}_R| = 1$ is dictated by the incident wave of amplitude unity. Above the resonance it behaves as a close cavity with $|\tilde{\varphi}_R| = 0$. These trends are robust whatever the water depth. Additional refinements would be necessary to restore the effect of wave dispersion which affects the amplitude within the resonator and the effect of the dock on its own.

4. Dynamics of the resonator in the transient regime

4.1. *Solutions for an incident wave packet in the transient signal*

We now move on to the dynamics of the resonator in the transient regime. As previously said, the solution of the reduced problem is still explicit. Given an incident wave packet

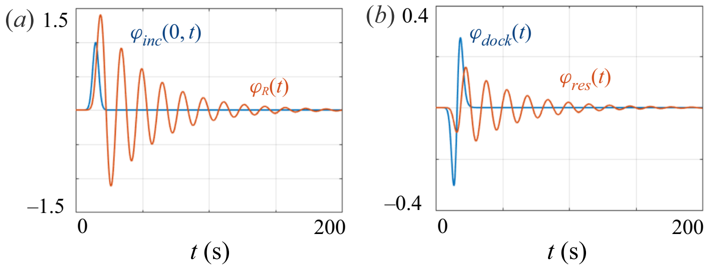

Figure 6. (*a*) Time variation of the amplitude $\varphi_R(t)$ within the resonator for an incident short pulse $\varphi_{inc}(0,t)$. (*b*) Resulting $\varphi_{res}(t)$ and $\varphi_{dock}(t)$ from (4.1*a,b*).

$\varphi_{inc}(x,t)$, the solution $\varphi_R(t)$ is known as it simply requires us to solve the equation of a damped oscillator forced with $\varphi_{inc}(0,t)$ in (2.11). We consider $\varphi_R(0,t=0)=\dot{\varphi}_R(0,t=0)=0$ as initial conditions corresponding to a source switched on at $t=0$. Next, we have from (2.7*a,b*) that

$$\varphi_{res}(t)=-\frac{2}{\omega_0^2\tau}\,\dot{\varphi}_R(t),\qquad \varphi_{dock}(t)=-\int_0^t \dot{\varphi}_{inc}(t')\mathrm{e}^{-(t-t')/\tau_{dock}}\,\mathrm{d}t', \tag{4.1a,b}$$

as $\varphi_{dock}(t=0)=0$. Eventually, the above solutions are used in (2.9*a,b*) to get the whole solution (2.6), with $\varphi^{\pm}(t)$ in (2.9*a,b*) the wave packets radiated by the resonator.

To begin with, we consider an incident short pulse of the form

$$\varphi_{inc}(0,t)=\mathrm{e}^{-\tau_f^{-2}(t-t_i)^2}, \tag{4.2}$$

with $\tau_f=3$ s (and $t_i=15$ s) whose significant spectral content is within the interval $\omega\in(0,2)$ rad s^{-1}. The pulse is much shorter than the damping time $\tau=38$ s, which provides a rough idea of the impulse response of the system. Figure 6(*a*) shows the incident pulse $\varphi_{inc}(0,t)$ and the resulting uniform potential within the cavity whose dynamics is that of an underdamped harmonic oscillator driven by $\varphi_{inc}(0,t)$. Panel (*b*) shows the corresponding variations of the radiated signals $\varphi_{res}(t)$ and $\varphi_{dock}(t)$, from (4.1*a,b*). Expectedly, we observe that $\varphi_{dock}(t)\simeq-\tau_{dock}\dot{\varphi}_{inc}(t)$ and thus it is as short as the initial pulse. In contrast, $\varphi_{res}(t)$ has a long regime of free oscillations, being weakly radiatively damped. To complete this representation, we report in figure 7 snapshots of the potential $\varphi(x,t)$ at the free surface and a profile for $t=120$ s. It is visible that the transmitted and reflected pulses resulting from the direct interaction with the incident pulse are followed by long right- and left-going wave trains radiated by the resonator (the segment $(0,L)$ is almost reduced to the origin in this representation).

We now inspect the ability of the HR to realize perfect transmission and perfect reflection in the transient regime. To do so, we use an incident wave packet able to excite more specifically a given frequency, namely we use

$$\varphi_{inc}(0,t)=a\exp(-\tau_f^{-2}(t-t_i)^2)\sin(\omega_f(t-t_i)), \tag{4.3}$$

with ω_f the forcing frequency, τ_f the width of the Gaussian envelope and a such that $\mathrm{Max}(\varphi_{inc}(0,t))=1$. We choose $\omega_f=\omega_1$ and $\omega_f=\omega_2$, the frequencies realizing perfect transmission and perfect reflection in the harmonic regime, from (3.6*a,b*); for comparison, we also consider $\omega_f=\omega_0$. For these 3 frequencies we set the incident pulse duration to $\tau_f=140$ s (approximately 40 oscillation periods). Results are shown in figure 8, where

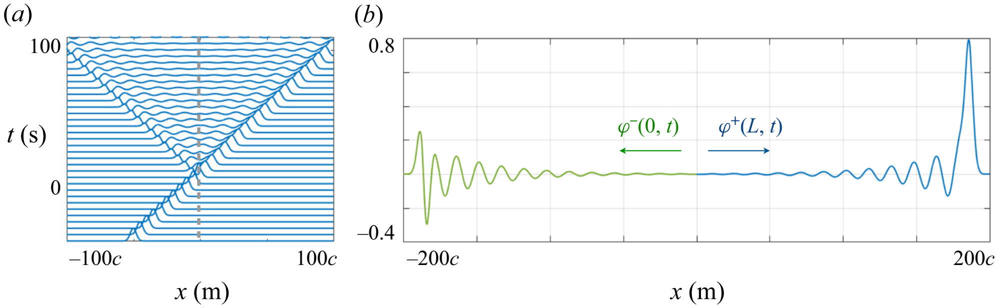

Figure 7. (*a*) Snapshots of the potential $\varphi(x, t)$ at the free surface, $x \notin (0, L)$, with $c = \sqrt{gH} \simeq 5.3\ \mathrm{m\ s^{-1}}$. (*b*) Profile of $\varphi(x, 120\ \mathrm{s})$; the oscillator emits $\varphi^+(0, t)$ and $\varphi^-(0, t)$.

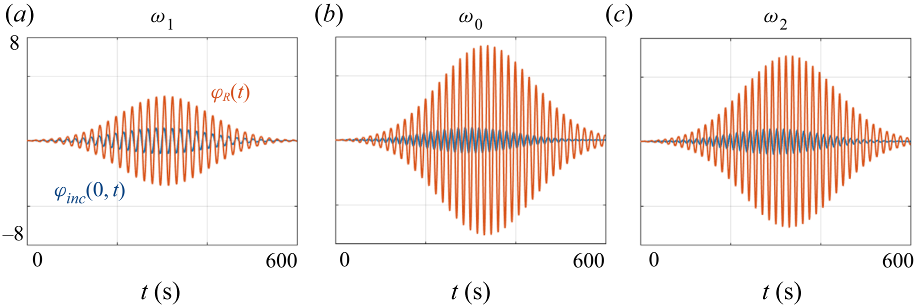

Figure 8. Incident pulse $\varphi_{inc}(0, t)$ from (4.3) (blue lines) and corresponding $\varphi_R(t)$ (red lines) (*a*) $\omega_f = \omega_1$ producing perfect transmission in the harmonic regime, (*b*) $\omega_f = \omega_0$ the resonance frequency and (*c*) ω_2 producing a perfect reflection in the harmonic regime (see (3.6*a*,*b*)).

we report $\varphi_{inc}(0, t)$ and the resulting $\varphi_R(t)$, and figure 9, where we report the snapshots of $\varphi(x, t)$ and a zoom on $\varphi_R(x, 600\ \mathrm{s})$. With a time scale variation of the incident pulse greater than the free oscillation period, the regime of oscillations driven by the forcing incident signal dominates and the free oscillation regime is almost negligible. Hence, both φ_{res} and φ_{dock} have almost the same duration as the incident wave packet and this is required in order to produce perfect transmission and perfect reflection. Indeed, perfect transmission results from destructive interference between the two radiated waves φ_{res} and φ_{dock} (hence $\varphi^- = 0$). Perfect reflection is in some sense more demanding as it results from destructive interference between φ_{res}, φ_{dock} and φ_{inc} as we want $\varphi^+ = 0$. As these conditions cannot be perfectly met, imperfect complete transmission and reflection are observed. Nevertheless, the enhancement in reflection for $\omega_f = \omega_1$ and in transmission for $\omega_f = \omega_2$ is visible when compared with the reference case at $\omega = \omega_0$.

5. Concluding remarks

We have studied an analogue of the acoustic HR in the context of water waves. As for its acoustic analogue, the lowest resonance is deeply subwavelength thanks to a thin neck connecting the cavity to the surrounding water. Obviously, this subwavelength property is of importance to the design of objects with the objective to control water waves of very long wavelength. The small dimensions of the whole device compared with the wavelength makes possible the use of asymptotic analysis and the derivation of a one-dimensional reduced model in the shallow water regime. The model has been validated in the harmonic

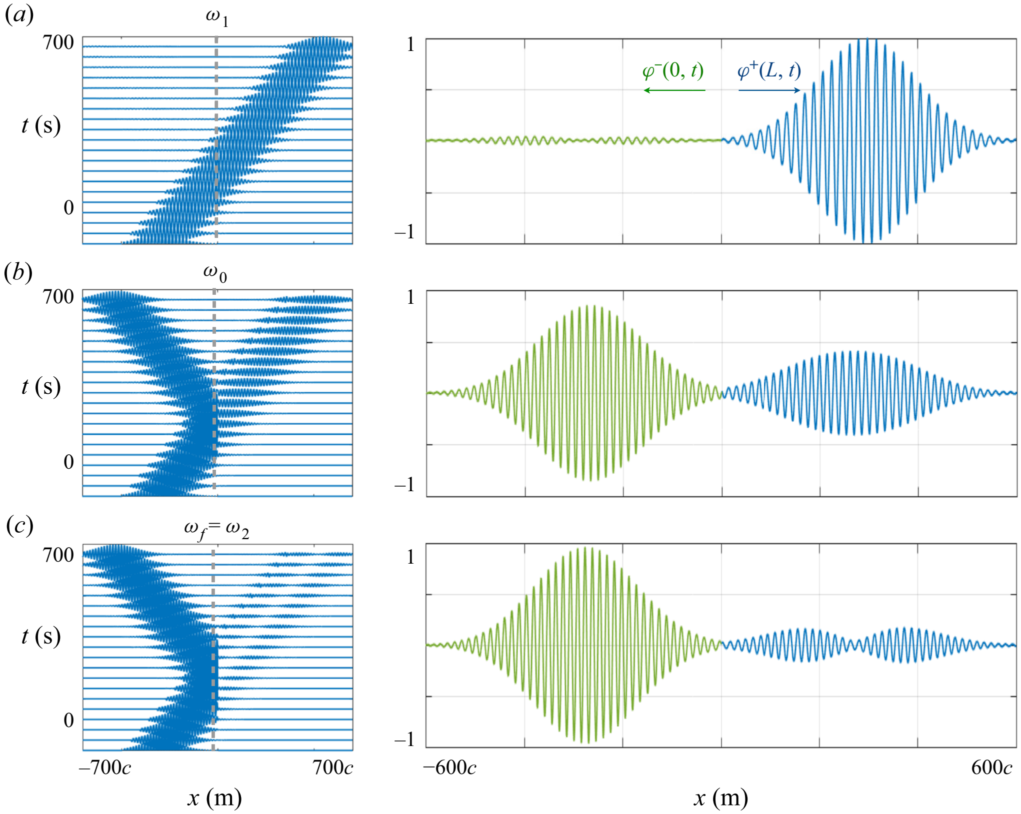

Figure 9. Same representation as in figure 7 for the three incident pulses of figure 8.

regime by comparison to direct numerics; afterwards, solutions in the transient regime have been sought.

The present analysis has been done in the idealized case of linear waves in an inviscid fluid; the resulting one-dimensional model corresponds to the dominant non-trivial asymptotic order. Within these assumptions, pursuing the calculations to the second order would allow us to capture more subtle effects such as the position of the neck connected to the cavity (here located on the bottom horizontal wall of the cavity but which can be positioned on a vertical wall, the two vertical walls playing a non-symmetric role for the incoming wave). Other extensions consist in including the effect of the losses due to the viscosity that we expect to be significant in the neck or due to nonlinearities within the cavity as the velocity reaches large values. Although this can be done by adding heuristically a damping term in the equation of the resonator (2.11), as in Monsalve *et al.* (2019), these ingredients can by explicitly accounted for in the analysis, see Caflisch *et al.* (1985) for viscous effects and Pham *et al.* (2020) for nonlinear effects. We have in mind the perfect absorption obtained with acoustic HRs (Romero-García *et al.* 2020) and for water waves in reflection (Monsalve *et al.* 2019). Another interesting extension would be to use a series of different resonators to obtain broadband behaviours (Jiménez *et al.* 2017; Bennetts *et al.* 2018).

Funding. V.P., P.P. and A.M. thank the supports of the start-up Bluerium. K.P. thanks the supports of the Agence de l'Innovation de Défense (AID) from the Direction Générale de l'Armement (DGA), under grant 2019 65 0070.

Declaration of interests. The authors report no conflict of interest.

Author ORCIDs.
Agnès Maurel https://orcid.org/0000-0001-8432-9871.

Author contributions. Conceptualization, L.-P.E.; theoretical model and numerical method, A.M., K.P.; writing of the manuscript, A.M. and K.P.; correction of the manuscript, L.-P.E., A.M., K.P., P.P., V.P. All authors have read and agreed to the published version of the manuscript.

Appendix A. Remark on the blockage coefficients and added lengths

Simple expressions for the effective length e_{eff} and blockage coefficient $\mathcal{B}$ are given here. What we need is the result of Tuck (1977), which provides the blockage coefficient of a step reducing the water depth from H^+ to $H^- < H^+$ (figure 10*a*). With $\mu = H^-/H^+$ it reads

$$\mathcal{B}_\mu = \frac{1}{\pi}\frac{(\mu^2+1)}{\mu}\log\frac{1+\mu}{1-\mu} - \frac{2}{\pi}\log\frac{4\mu}{1-\mu^2}. \tag{A1}$$

This coefficient appears in the jump of the potential which reads as $(\varphi^+ - \varphi^-) = \mathcal{B}_\mu D$ at the section discontinuity while the flow rate is continuous $D = H^+\partial_x\varphi^+ = H^-\partial_x\varphi^-$. Owing to this result, it is possible to extrapolate the blockage coefficient $\mathcal{B}$ in problem (*b*) and the effective length e_{eff} in problem (*c*) of figure 10.

We begin with problem (*b*). As the effect of the evanescent fields at $x = 0$ and $x = L$ is encapsulated in $\mathcal{B}_\mu$, the solution can be written

$$\varphi(x<0) = \frac{x}{H}, \quad \varphi(0<x<L) = \frac{x}{h^-} + \alpha, \quad \varphi(x>L) = \frac{(x-L)}{H} + \mathcal{B}, \tag{A2a–c}$$

which already satisfies the continuity of the flow rate $D = 1$. Applying further $\varphi(0^+) - \varphi(0^-) = \mathcal{B}_\mu$ and $\varphi(L^+) - \varphi(L^-) = \mathcal{B}_\mu$, we obtain $\alpha = \mathcal{B}_\mu$ and

$$\mathcal{B} = \frac{L}{h^-} + 2\mathcal{B}_\mu, \quad \mu = \frac{h^-}{H}. \tag{A3a,b}$$

We now move on to problem (*c*), which is the problem involving the added length in the neck of the resonator (we used mirror symmetry). We do the same as previously with

$$\varphi(x<0) = \frac{2x}{L}, \quad \varphi(0<x<e) = \frac{2x}{\ell} + \beta, \quad \varphi(x>e) = \frac{(x-e)}{L_o} + \mathcal{B}_N, \tag{A4a–c}$$

which satisfies $D = 1$. Applying further $\varphi(0^+) - \varphi(0^-) = \mathcal{B}_\mu$ (with $\mu = \ell/L$) and $\varphi(e^+) - \varphi(e^-) = \mathcal{B}_{\mu_0}$ (with $\mu_0 = \ell/L_o$), we obtain $\beta = \mathcal{B}_\mu$ and

$$\mathcal{B}_N = \frac{2e}{\ell} + \mathcal{B}_\mu + \mathcal{B}_{\mu_0}, \quad \mu = \frac{\ell}{L}, \quad \mu_0 = \frac{\ell}{L_o}. \tag{A5a–c}$$

Next, the effective length e_{eff} is by definition the length such that the constant velocity in $(0, e)$ satisfies

$$v|_N = \frac{2}{\ell} = \frac{\varphi(e^+) - \varphi(0^-)}{e_{\mathit{eff}}}, \tag{A6}$$

which implies

$$e_{\mathit{eff}} = \frac{\ell}{2}\mathcal{B}_N = e + \frac{\ell}{2}\left(\mathcal{B}_\mu + \mathcal{B}_{\mu_0}\right). \tag{A7}$$

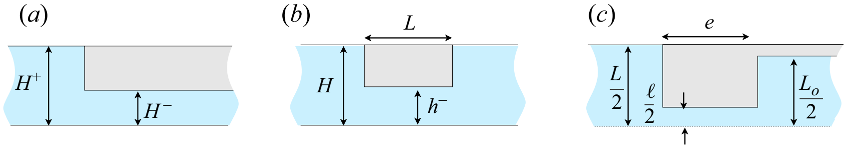

Figure 10. (*a*) The problem of a perfect fluid flowing in a rigid duct with a sudden change in height ($H^+ \rightarrow H^-$) involving the blockage coefficient $\mathcal{B}_\mu$, $\mu = H^-/H^+$. (*b*) The problem of a perfect fluid flowing in a rigid duct with two sudden changes in height $H \rightarrow h^- \rightarrow H$ involves a blockage coefficient $\mathcal{B}$. (*c*) The problem of a perfect fluid flowing through a duct with three sudden changes in height ($L \rightarrow \ell \rightarrow L_o$) involves a blockage coefficient $\mathcal{B}_n$.

The above result is consistent with the analysis of Mercier, Marigo & Maurel (2017) (owing to $\mathcal{B}_\mu \simeq -(2/\pi)\log(\sin((\pi/2)\mu))$). It is worth noting that the blockage coefficient in (A3*a*,*b*) appears explicitly in the asymptotic analysis, see (B26*a*–*b*). In contrast, the effective length (A7) is introduced heuristically as the analysis provides only the actual length of the neck, see (B46*a*,*b*) (an effective length would appear at the following asymptotic order).

Appendix B. Asymptotic analysis

In this section, we shall derive the reduced model (2.3) thanks to asymptotic analysis. This will be done by defining a small parameter ε and by choosing scalings for all the dimensions of the problem.

B.1. *The choice of the scalings*

The heuristic calculation leading to (1.2) is used to set the scalings. This calculation is done assuming that the cavity has dimensions much smaller than the incident wavelength, and that the cavity is disconnected from the surrounding fluid, resulting in a zero velocity and a constant potential at the dominant order. What we want to obtain with the scalings is that the non-dimensional frequency remains of the order of the resonance frequency asymptotically. In the most general case, defining $\varepsilon = kD$ with D, a measure of the cavity extent, this means

$$\frac{\omega_0}{c}D = \frac{D}{c}\sqrt{\frac{g\ell}{eL_o}} = O(\varepsilon), \tag{B1}$$

with c the velocity of the water waves. The above relation holds for a wave in shallow to deep water. In our study, we focus on the shallow water regime where $c = \sqrt{gH}$ and we assume that H and the dimensions of the cavity (L, L_o, h^+) tend to 0 as fast as H when ε vanishes. Defining $\varepsilon = kH$, we obtain that the geometry of the neck must satisfy

$$\sqrt{\frac{\ell}{e}} = O(\varepsilon). \tag{B2}$$

This means that ℓ has to decrease faster than e when $\varepsilon \rightarrow 0$ and the simplest scaling to guarantee this is given by $ke = O(\varepsilon)$ and $k\ell = O(\varepsilon^3)$. We thus expect that the fields have variations associated with three scales, the macroscopic wavelength scale, the mesoscopic scales being the typical scale of the dock and the microscopic scale associated with the neck opening.

B.2. *Non-dimensional formulation*

We use a non-dimensional problem by setting $t \to \omega t$, $\boldsymbol{x} \to k\boldsymbol{x}$, $\boldsymbol{u} \to \boldsymbol{u}/U_0$ and $\phi \to k\phi/U_0$, with $k = \omega/\sqrt{gH}$ and U_0 a characteristic velocity. The result consists in finding the potential ϕ and the velocity field $\boldsymbol{u} = (u, v)$ such that (2.1)–(2.2*a,b*) read

$$\begin{cases} \operatorname{div} \boldsymbol{u} = \boldsymbol{0}, \quad \boldsymbol{u} = \nabla\phi, \\ v|_{z=0} = -\varepsilon\partial_{tt}\phi, \quad \boldsymbol{u}\cdot\boldsymbol{n}|_{\varGamma} = 0, \end{cases} \tag{B3}$$

where $\varepsilon = \omega\sqrt{H/g} \ll 1$ is a small parameter.

B.3. *The different regions and their matchings*

B.3.1. *The regions far from and near the resonator*

(i) *The macroscopic region far from the resonator*

The macroscopic region corresponds to the region far from the resonator where the evanescent field is negligible and the fields vary at the scale of the incident wavelength. There, we rescale the vertical coordinate due to the shallowness hypothesis introducing $z_m = z/\varepsilon$ and we expand the potential and the velocity as

$$\phi = \phi^0(x, z_m, t) + \varepsilon\phi^1(x, z_m, t) + \cdots, \quad \boldsymbol{u} = \boldsymbol{u}^0(x, z_m, t) + \varepsilon\boldsymbol{u}^1(x, z_m, t) + \cdots, \tag{B4a,b}$$

with $\boldsymbol{u}^i = (u^i, v^i)$. In this region, the differential operators read

$$\nabla f = \partial_x f\boldsymbol{e}_x + \varepsilon^{-1}\partial_{z_m} f\boldsymbol{e}_z, \quad \operatorname{div}\boldsymbol{f} = \partial_x f_x + \varepsilon^{-1}\partial_{z_m} f_z. \tag{B5a,b}$$

(ii) *The mesoscopic regions, near the resonator but far from its neck*

The resonator has a characteristic size, apart of the neck, satisfying $kh^+ \sim \varepsilon$ and $kL \sim \varepsilon$. Accordingly, we introduce the mesoscopic space variable $(x_m, z_m) = (x/\varepsilon, z/\varepsilon)$. Near the resonator and far from the neck, we distinguish two different mesoscopic regions. One is an unbounded domain $\hat{\varOmega}_m$ outside the resonator and the other is the bounded domain $\check{\varOmega}_m$ of the resonator cavity (figure 11). Accordingly we consider the two asymptotic expansions

$$\begin{cases} \phi = \hat{\phi}^0_m(x_m, z_m, t) + \varepsilon\hat{\phi}^1_m(x_m, z_m, t) + \cdots, \quad \boldsymbol{u} = \hat{\boldsymbol{u}}^0_m(x_m, z_m, t) + \varepsilon\hat{\boldsymbol{u}}^1_m(x_m, z_m, t) + \cdots, \\ \phi = \check{\phi}^0_m(x_m, z_m, t) + \varepsilon\check{\phi}^1_m(x_m, z_m, t) + \cdots, \quad \boldsymbol{u} = \check{\boldsymbol{u}}^0_m(x_m, z_m, t) + \varepsilon\check{\boldsymbol{u}}^1_m(x_m, z_m, t) + \cdots, \end{cases} \tag{B6}$$

with $\hat{\boldsymbol{u}}^i_m = (\hat{u}^i_m, \hat{v}^i_m)$ and $\check{\boldsymbol{u}}^i_m = (\check{u}^i_m, \check{v}^i_m)$, and the connection between them will be obtained through an asymptotic analysis in the vicinity of the neck. In these regions, the differential operators read

$$\nabla f = \varepsilon^{-1}\nabla_m f, \quad \operatorname{div}\boldsymbol{f} = \varepsilon^{-1}\operatorname{div}_m\boldsymbol{f}. \tag{B7a,b}$$

(iii) *Along the neck and at its ends*

The neck is thin and long and this is accounted for by setting $ke \sim \varepsilon$ and $k\ell \sim \varepsilon^3$. By zooming on the neck, we have thus to distinguish three different regions: inside the neck i.e. far from its ends, near the top end and near the bottom end. We introduce the microscopic space variables $(x_\mu, z_\mu) = (x/\varepsilon^3, z/\varepsilon^3)$. Inside the neck, we define the

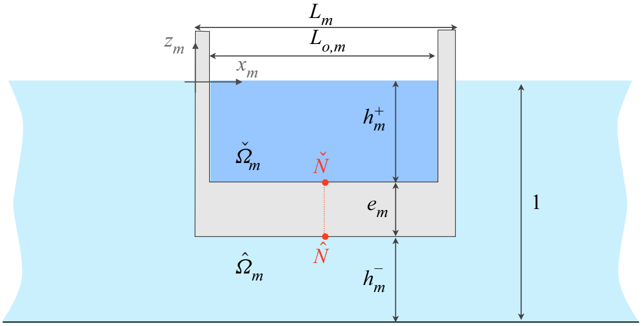

Figure 11. The two mesoscopic regions: $\hat{\Omega}_m$ being the unbounded region outside the cavity and $\check{\Omega}_m$ the bounded region within the cavity. The ends of the neck are reduced to the points $\hat{N}$ and $\check{N}$ at this scale. The lengths are rescaled with H, hence $d_m = d/H = O(1)$, for $d = L, L_o, h^+, h^-, e$.

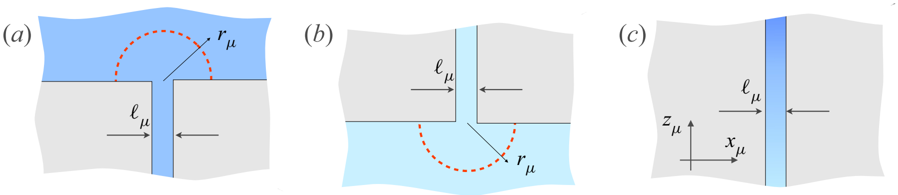

Figure 12. The three microscopic regions: (*a*) in the vicinity of the top of the neck, (*b*) in the vicinity of the bottom of the neck and (*c*) within the neck far from its ends. The rescaled coordinates are Cartesian coordinates (x_μ, z_μ) and polar coordinates r_μ, and $\ell_\mu = \ell/(\varepsilon^2 H)$. The velocity is radial and singular at both ends in (*a*,*b*).

expansions

$$\phi = \phi_\mu^0(x_\mu, z_m, t) + \varepsilon\phi_\mu^1(x_\mu, z_m, t) + \cdots, \quad \boldsymbol{u} = \varepsilon^{-1}\boldsymbol{u}_\mu^{-1}(x_\mu, z_m, t) + \boldsymbol{u}_\mu^0(x_\mu, z_m, t) + \cdots, \tag{B8a,b}$$

with $\boldsymbol{u}_\mu^i = (u_\mu^i, v_\mu^i)$ and

$$\nabla f = \varepsilon^{-3}\partial_{x_\mu} f \boldsymbol{e}_x + \varepsilon^{-1}\partial_{z_m} f \boldsymbol{e}_z, \quad \operatorname{div}\boldsymbol{f} = \varepsilon^{-3}\partial_{x_\mu} f_x + \varepsilon^{-1}\partial_{z_m} f_z. \tag{B9a,b}$$

Near the top end and bottom end of the neck, we use

$$\begin{cases} \phi = \hat{\phi}_\mu^0(x_\mu, z_\mu, t) + \varepsilon\hat{\phi}_\mu^1(x_\mu, z_\mu, t) + \cdots, & \boldsymbol{u} = \varepsilon^{-1}\hat{\boldsymbol{u}}_\mu^{-1}(x_\mu, z_\mu, t) + \hat{\boldsymbol{u}}_\mu^0(x_\mu, z_\mu, t) + \cdots, \\ \phi = \check{\phi}_\mu^0(x_\mu, z_\mu, t) + \varepsilon\check{\phi}_\mu^1(x_\mu, z_\mu, t) + \cdots, & \boldsymbol{u} = \varepsilon^{-1}\check{\boldsymbol{u}}_\mu^{-1}(x_\mu, z_\mu, t) + \check{\boldsymbol{u}}_\mu^0(x_\mu, z_\mu, t) + \cdots, \end{cases} \tag{B10}$$

with $\hat{\boldsymbol{u}}_\mu^i = (\hat{u}_\mu^i, \hat{v}_\mu^i)$ and $\check{\boldsymbol{u}}_\mu^i = (\check{u}_\mu^i, \check{v}_\mu^i)$ (figure 12), and

$$\nabla f = \varepsilon^{-3}\nabla_\mu f, \quad \operatorname{div}\boldsymbol{f} = \varepsilon^{-3}\operatorname{div}_\mu \boldsymbol{f}. \tag{B11a,b}$$

Note that we start the expansions for the velocity at the order ε^{-1} to match the resonant behaviour of the cavity (other choices would lead to inconsistencies).

B.3.2. *Matching conditions*

(i) *Macro-meso matching conditions*

The matching conditions are obtained by matching the expansions (B4*a*,*b*) and (B6) in an intermediate region where $x = \varepsilon x_m \to 0^\pm$ and $x_m \to \pm\infty$, namely

$$\phi^0(x, z_m, t) + \varepsilon\phi^1(x, z_m, t) + \cdots \underset{x\to 0^\pm, x_m\to\pm\infty}{\sim} \hat{\phi}^0_m(x_m, z_m, t) + \varepsilon\hat{\phi}^1_m(x_m, z_m, t) + \cdots . \tag{B12}$$

Using Taylor expansions of $\phi^0(\varepsilon x_m, z_m)$ for $\varepsilon x_m \to 0^\pm$ provides the matching conditions at the first two orders

$$\lim_{x_m\to\pm\infty} \hat{\phi}^0_m = \phi^0|_{x=0^\pm}, \quad \lim_{x_m\to\pm\infty} \left(\hat{\phi}^1_m - x_m\partial_x\phi^0|_{x=0^\pm}\right) = \phi^1|_{x=0^\pm}. \tag{B13a,b}$$

The same applies for the velocity, namely

$$\lim_{x_m\to\pm\infty} \hat{\boldsymbol{u}}^0_m = \boldsymbol{u}^0_{x=0^\pm}, \quad \lim_{x_m\to\pm\infty} \left(\hat{\boldsymbol{u}}^1_m - x_m\partial_x\boldsymbol{u}^0{}_{x=0^\pm}\right) = \boldsymbol{u}^1_{x=0^\pm}. \tag{B14a,b}$$

(ii) *Meso-micro matching conditions*

Due to the possible singular behaviour of the fields at the ends of the neck, explicit matching conditions cannot be derived *a priori* as simply as in the macro-meso case. This has to be done on a case-by-case basis but the procedure stays the same. It consists in matching the expansions (B6) and (B10) in intermediate regions near the points $\hat{N}$ and $\check{N}$. Introducing the mesoscopic polar coordinate (r_m, t) and the microscopic polar coordinate (r_μ, t) with $r_\mu = r_m/\varepsilon^2$, it consists of enforcing for the potentials

$$\left.\begin{aligned} &\forall\theta \in (0, \pi), \quad \check{\phi}^0_m + \varepsilon\check{\phi}^1_m + \cdots \underset{\substack{r_m\to 0\\ r_\mu\to+\infty}}{\sim} \check{\phi}^0_\mu + \varepsilon\check{\phi}^1_\mu + \cdots ,\\ &\forall\theta \in (\pi, 2\pi), \quad \hat{\phi}^0_m + \varepsilon\hat{\phi}^1_m + \cdots \underset{\substack{r_m\to 0\\ r_\mu\to+\infty}}{\sim} \hat{\phi}^0_\mu + \varepsilon\hat{\phi}^1_\mu + \cdots , \end{aligned}\right\} \tag{B15}$$

as well as for the velocities

$$\left.\begin{aligned} &\forall\theta \in (0, \pi), \quad \check{\boldsymbol{u}}^0_m + \varepsilon\check{\boldsymbol{u}}^1_m + \cdots \underset{\substack{r_m\to 0\\ r_\mu\to+\infty}}{\sim} \varepsilon^{-1}\check{\boldsymbol{u}}^{-1}_\mu + \check{\boldsymbol{u}}^0_\mu + \cdots ,\\ &\forall\theta \in (\pi, 2\pi), \quad \hat{\boldsymbol{u}}^0_m + \varepsilon\hat{\boldsymbol{u}}^1_m + \cdots \underset{\substack{r_m\to 0\\ r_\mu\to+\infty}}{\sim} \varepsilon^{-1}\hat{\boldsymbol{u}}^{-1}_\mu + \hat{\boldsymbol{u}}^0_\mu + \cdots . \end{aligned}\right\} \tag{B16}$$

(iii) *Micro-matching conditions between the neck and its ends*

Inside the neck, the expansions (B8*a*,*b*) have to match the expansions (B10) at its ends. By using Taylor expansions near the ends of the neck with $z_m = \varepsilon^2 z_\mu - h^+_m$ near $\check{N}$ and $z_m = \varepsilon^2 z_\mu - (h^+_m + e_m)$ near $\hat{N}$, we get for $x_\mu \in (0, \ell_\mu)$

$$\left.\begin{aligned} &i = 0, 1, \quad \lim_{z_\mu\to-\infty} \check{\phi}^i_\mu = \phi^i_\mu|_{z_m=-h^+_m}, \quad \lim_{z_\mu\to+\infty} \hat{\phi}^i_\mu = \phi^i_\mu|_{z_m=-(h^+_m+e_m)},\\ &i = -1, 0, \quad \lim_{z_\mu\to-\infty} \check{\boldsymbol{u}}^i_\mu = \boldsymbol{u}^i_\mu|_{z_m=-h^+_m}, \quad \lim_{z_\mu\to+\infty} \hat{\boldsymbol{u}}^i_\mu = \boldsymbol{u}^i_\mu|_{z_m=-(h^+_m+e_m)}. \end{aligned}\right\} \tag{B17}$$

B.4. *Effective equations far from the resonator*

Far from the resonator, we derive asymptotically the shallow water equations at orders 0 and 1 which read

$$i = 0, 1, \quad \partial_x u^i(x, t) - \partial_{tt}\phi^i(x, t) = 0, \quad u^i = \partial_x \phi^i, \tag{B18a–c}$$

where u^i and ϕ^i do not depend on z_m. To do so, we shall use (B4*a,b*) in (B3) along with (B5*a,b*). At the dominant order ε^{-1} we get that $\partial_{z_m} v^0 = 0$, $\partial_{z_m}\phi^0 = 0$. Hence, ϕ^0 and v^0 do not depend on z_m and $v^0 = 0$, as $v^0(x, 0) = 0$. At the order ε^0, we have

$$\partial_x u^0 + \partial_{z_m} v^1 = 0, \quad u^0 = \partial_x \phi^0, \tag{B19a,b}$$

which we integrate along z_m using $v^1(x, -1, t) = 0$ and $v^1(x, 0, t) = -\partial_{tt}\phi^0(x, t)$ which provides (B18*a–c*) for $i = 0$. At this order, we also have that ϕ^1 does not depend on z_m as $v^0 = \partial_{z_m}\phi^1 = 0$. It follows that we have the same sequence of equations, with $\partial_x u^1 + \partial_{z_m} v^2 = 0$, $u^1 = \partial_x \phi^1$, resulting in (B18*a–c*) for $i = 1$. At this stage, the missing information is the transmission conditions near the origin where the resonator is located.

B.5. *Effective transmission conditions through the resonator*

We shall now derive the effective transmission conditions across the resonator at the first two orders to complete the wave equation obtained in the previous part.

B.5.1. *Continuity conditions at order 0*

In the mesoscopic region $\hat{\varOmega}_m$ outside the resonator, we use (B6) in (B3) along with (B7*a,b*). We obtain at the order ε^{-1} that $\nabla_m \hat{\phi}^0_m = \mathbf{0}$, hence $\hat{\phi}^0_m$ is spatially homogeneous in $\hat{\varOmega}_m$. Using the matching conditions (B13*a,b*), we deduce that the potential $\phi^0(x, t)$ is continuous at $x = 0$ with

$$\hat{\phi}^0_m(t) = \phi^0(0^\pm, t), \quad \text{or} \quad [\![\phi^0]\!]_0 \equiv \phi^0(0^+, t) - \phi^0(0^-, t) = 0. \tag{B20a,b}$$

With $\hat{D}_m = \{x_m \in (-\infty, 0) \cup (L_m, +\infty), z_m = 0\}$, we also have at this order

$$\mathrm{div}_m\, \hat{\boldsymbol{u}}^0_m = 0, \quad \hat{v}^0_m|_{\hat{D}_m} = 0, \quad \hat{\boldsymbol{u}}^0_m|_{\hat{\varGamma}} \cdot \boldsymbol{n} = 0, \tag{B21a–c}$$

that we integrate over $\hat{\varOmega}_m \cap \{(-x^*_m, x^*_m) \times (-1, 0)\}$ with $x^*_m > L_m$. As $\hat{\boldsymbol{u}}^0_m$ is regular at the point $\hat{N} = (0, -(h^+_m + e_m))$, we get

$$\int_{-1}^{0} \hat{u}^0_m(x^*_m, z_m, t)\, \mathrm{d}z_m - \int_{-1}^{0} \hat{u}^0_m(-x^*_m, z_m, t)\, \mathrm{d}z_m = 0. \tag{B22}$$

Now passing to the limit when $x^*_m \to +\infty$ and using the matching conditions (B13*a,b*), we get the continuity of the horizontal velocity

$$[\![u^0]\!]_0 = 0. \tag{B23}$$

Thus, from (B20*a,b*)–(B23), the resonator is not seen at the dominant order and we have to go to the next order to capture its effect.

B.5.2. *Jump condition on the potential at order 1*

At the next order, to get the transmission conditions on ϕ^1, we have to solve the mesoscopic problem on $(\hat{\phi}^1_m, \hat{\boldsymbol{u}}^0_m)$ given by

$$\mathrm{div}_m\, \hat{\boldsymbol{u}}^0_m = 0, \quad \hat{\boldsymbol{u}}^0_m = \nabla_m \hat{\phi}^1_m, \quad \hat{v}^0_m|_{\hat{D}_m} = 0, \quad \hat{\boldsymbol{u}}^0_m|_{\hat{\Gamma}} \boldsymbol{\cdot} \boldsymbol{n} = 0, \quad \lim_{x_m \to \pm\infty} \hat{\boldsymbol{u}}^0_m \to u^0(0, t)\boldsymbol{e}_x. \tag{B24a–e}$$

The limits of $\hat{\boldsymbol{u}}^0_m$ for $x_m \to \pm\infty$ correspond to (B14a,b) using from § B.4 that $\boldsymbol{u}^0(0, t) = u^0(0, t)\boldsymbol{e}_x$. The solution of this problem is linear with respect to $u^0(0, t)$ hence we set

$$\hat{\phi}^1_m(\boldsymbol{x}_m, t) = u^0(0, t)P(\boldsymbol{x}_m) + \bar{\phi}^1(t), \tag{B25}$$

with the elementary static field $P(\boldsymbol{x}_m)$ given by

$$\Delta_m P = 0, \quad \partial_{z_m} P|_{\hat{D}_m} = 0, \quad \nabla_m P|_{\hat{\Gamma}} \boldsymbol{\cdot} \boldsymbol{n} = 0, \quad \lim_{x_m \to \pm\infty} \nabla_m P \to \boldsymbol{e}_x, \tag{B26a–d}$$

and $\bar{\phi}^1(t)$ is introduced as $\hat{\phi}^1_m$ is known up to a function of the time. The behaviours at infinity of $P(\boldsymbol{x}_m)$ read

$$P(\boldsymbol{x}_m) \underset{x_m \to -\infty}{\sim} x_m, \quad P(\boldsymbol{x}_m) \underset{x_m \to +\infty}{\sim} (x_m - L_m) + \mathcal{B}, \tag{B27a,b}$$

where $\mathcal{B}$ is a blockage coefficient independent of the macroscopic loading and depending only on the external geometry of the resonator; it is the contribution of the dock problem only. Now, recalling the macroscopic relation (B18a–c) and passing to the limit in (B25), we get $\lim_{x_m \to -\infty}(\hat{\phi}^1_m - \partial_x \phi^0(0, t)x_m) = \bar{\phi}^1(t)$ and $\lim_{x_m \to +\infty}(\hat{\phi}^1_m - \partial_x \phi^0(0, t)x_m) = \bar{\phi}^1(t) + (\mathcal{B} - L_m)u^0(0, t)$. In virtue of the matching conditions (B13a,b), we deduce that

$$[\![\phi^1]\!]_0 = (\mathcal{B} - L_m)u^0(0, t). \tag{B28}$$

B.5.3. *Jump condition on the velocity at order 1*

(i) *Preliminaries*

Contrary to $\hat{\boldsymbol{u}}^0_m$ which was assumed to be regular in the vicinity of $\hat{N}$, $\hat{\boldsymbol{u}}^1_m$ is singular near $\hat{N}$ due to the neck, hence a specific treatment is required. Integrating as previously the incompressibility equation $\mathrm{div}_m\, \hat{\boldsymbol{u}}^1_m = 0$, over $\hat{\Omega}_m \cap \{(-x^*_m, x^*_m) \times (-1, 0)\}$ and taking into account the boundary conditions $\hat{\boldsymbol{u}}^1_m \boldsymbol{\cdot} \boldsymbol{n} = 0$ on the rigid boundaries (excluding a vanishing region near $\hat{N}$) and $\hat{v}^1_m(x_m, z_m = 0, t) = -\partial_{tt}\hat{\phi}^0_m(t)$ at the free surface for $x_m \in (-x^*_m, 0)$ and for $x_m \in (L_m, x^*_m)$, we obtain

$$\int_{-1}^{0} \hat{u}^1_m|_{x^*_m}\, \mathrm{d}z_m - \int_{-1}^{0} \hat{u}^1_m|_{-x^*_m}\, \mathrm{d}z_m - (2x^*_m - L_m)\partial_{tt}\hat{\phi}^0_m(t) - \int_{\pi}^{2\pi} r_m \hat{\boldsymbol{u}}^1_m \boldsymbol{\cdot} \boldsymbol{e}_r\, \mathrm{d}t = 0. \tag{B29}$$

Note that despite the singular behaviour of $\hat{\boldsymbol{u}}^1_m$, the contour integral near $\hat{N}$, has to be finite. Knowing from (B18a–c) and (B20a,b) that $\partial_{tt}\hat{\phi}^0_m(t) = \partial_{tt}\phi^0(0, t) = \partial_x u^0(0, t)$, we can apply the matching conditions on the velocities at order 1 in (B14a,b). Passing to the limit when $x_m^* \rightarrow +\infty$ and when $r_m \rightarrow 0$ finally gives

$$[\![u^1]\!]_0 = -L_m \partial_x u^0(0, t) + \lim_{r_m \rightarrow 0} \int_{\pi}^{2\pi} r_m \hat{\boldsymbol{u}}_m^1(r_m, t, t) \cdot \boldsymbol{e}_r \, \mathrm{d}t. \tag{B30}$$

While in the absence of a neck, $\hat{\boldsymbol{u}}_m^1$ is regular and the last term in (B30) vanishes; in the present case, the finiteness of the contour integral in (B30) imposes that

$$\hat{\boldsymbol{u}}_m^1 \underset{r_m \rightarrow 0}{\sim} \frac{\hat{A}(t)}{r_m} \boldsymbol{e}_r, \quad \longrightarrow \quad [\![u^1]\!]_0 = -L_m \partial_x u^0(0, t) + \pi \hat{A}(t). \tag{B31}$$

The determination of $\hat{A}(t)$ will be obtained from the matching with the neck region, see forthcoming (B48).

(ii) *Inside the resonant cavity* Inside the cavity at the mesoscopic scale, we have at the dominant order that

$$\boldsymbol{\nabla}_m \check{\phi}_m^0 = 0, \quad \longrightarrow \quad \check{\phi}_m^0(t) \tag{B32}$$

is homogeneous inside the cavity. At the next order, the problem in $\check{\phi}_m^1$ is given by

$$\mathrm{div}_m \, \check{\boldsymbol{u}}_m^0 = 0, \quad \check{\boldsymbol{u}}_m^0 = \boldsymbol{\nabla}_m \check{\phi}_m^1, \quad \check{\boldsymbol{u}}_m^0|_{\check{\Gamma}} \cdot \boldsymbol{n} = 0, \quad \check{v}_m^0(x_m, 0, t) = 0, \tag{B33a–d}$$

where $\check{\boldsymbol{u}}_m^0$ is assumed to be regular near $\check{N}$. Multiplying $\mathrm{div}_m \, \check{\boldsymbol{u}}_m^0 = 0$ by $\check{\phi}_m^1$, integrating by parts over $\check{\Omega}_m$ and using the Neumann boundary conditions on the whole contour of $\check{\Omega}_m$ gives $\int_{\check{\Omega}_m} \check{\boldsymbol{u}}_m^0 \cdot \check{\boldsymbol{u}}_m^0 \, \mathrm{d}\boldsymbol{x}_m = 0$. Therefore, we have that

$$\check{\boldsymbol{u}}_m^0 = \boldsymbol{0}, \quad \text{hence } \check{\phi}_m^1(t) \tag{B34}$$

is uniform inside the cavity. Going to the next order, we have

$$\mathrm{div}_m \, \check{\boldsymbol{u}}_m^1 = 0, \quad \check{\boldsymbol{u}}_m^1|_{\check{\Gamma}} \cdot \boldsymbol{n} = 0, \quad \check{v}_m^1(x_m, 0, t) = -\partial_{tt} \check{\phi}_m^0(t), \tag{B35a–c}$$

which we integrate over $\check{\Omega}_m$, excluding as previously a vanishing region near $\check{N}$. We obtain

$$-\int_0^{\pi} r_m \check{\boldsymbol{u}}_m^1(r_m, \theta, t) \cdot \boldsymbol{e}_r \, \mathrm{d}\theta - L_{o,m} \partial_{tt} \check{\phi}_m^0(t) = 0. \tag{B36}$$

To accommodate the above equation, $\check{\boldsymbol{u}}_m^1$ must be singular near $\check{N}$ with

$$\check{\boldsymbol{u}}_m^1 \underset{r_m \rightarrow 0}{\sim} \frac{\check{A}(t)}{r_m} \boldsymbol{e}_r, \quad \check{A}(t) = -\frac{L_{o,m}}{\pi} \partial_{tt} \check{\phi}_m^0(t). \tag{B37a,b}$$

(iii) *Matching conditions at the tips of the neck*

We now analyse the behaviour in the microscopic regions at the top end and the bottom ends of the neck. To do so, we use (B10) in (B3) along with (B11a,b). In both regions, since the velocities start at the order -1, we have at the dominant orders that

$$i = 0, 1 \quad \boldsymbol{\nabla}_\mu \check{\phi}_\mu^i = \boldsymbol{\nabla}_\mu \hat{\phi}_\mu^i = \boldsymbol{0}, \quad \text{hence } \check{\phi}_\mu^i(t), \ \hat{\phi}_\mu^i(t) \tag{B38}$$

are homogeneous in their respective microscopic regions. In virtue of the matching conditions (B13a,b) and using (B20a,b), we deduce that

$$\hat{\phi}_\mu^0(t) = \hat{\phi}_m^0(t) = \phi^0(0, t). \tag{B39}$$

Next, the incompressibility equations at the dominant order read

$$\mathrm{div}_\mu \, \check{\boldsymbol{u}}_\mu^{-1} = 0, \quad \mathrm{div}_\mu \, \hat{\boldsymbol{u}}_\mu^{-1} = 0. \tag{B40a,b}$$

The velocities at these microscopic scales have to match the velocities at the mesoscopic scales as stated in (B16). With $\hat{\boldsymbol{u}}_m^1$ given by (B31) and $\check{\boldsymbol{u}}_m^1$ given by (B37a,b) and owing to

$r_m = \varepsilon^2 r_\mu$ in (B16) we obtain

$$\forall\theta \in (0, \pi), \quad \check{\boldsymbol{u}}_\mu^{-1} \underset{r_\mu \to +\infty}{\sim} \frac{\check{A}(t)}{r_\mu}\boldsymbol{e}_r, \quad \forall\theta \in (\pi, 2\pi), \quad \hat{\boldsymbol{u}}_\mu^{-1} \underset{r_\mu \to +\infty}{\sim} \frac{\hat{A}(t)}{r_\mu}\boldsymbol{e}_r. \tag{B41a–d}$$

We can now integrate the incompressibility equations (B40a,b) over $\hat{\Omega}_\mu$ and $\check{\Omega}_\mu$. By applying Neumann boundary conditions on the walls, using the asymptotic behaviours (B41a–d) at infinity as well as the matching conditions (B10) with the neck, we get

$$\left.\begin{aligned} \lim_{z_\mu \to -\infty} \int_0^{\ell_\mu} \check{v}_\mu^{-1}(x_\mu, z_\mu, t)\,\mathrm{d}x_\mu &= \lim_{r_\mu \to +\infty} \int_0^{\pi} \check{\boldsymbol{u}}_\mu^{-1} \boldsymbol{\cdot} \boldsymbol{e}_r = \pi\check{A}(t), \\ \lim_{z_\mu \to +\infty} \int_0^{\ell_\mu} \hat{v}_\mu^{-1}(x_\mu, z_\mu)\, dx_\mu &= -\lim_{r_\mu \to +\infty} \int_\pi^{2\pi} \hat{\boldsymbol{u}}_\mu^{-1} \boldsymbol{\cdot} \boldsymbol{e}_r = -\pi\hat{A}. \end{aligned}\right\} \tag{B42}$$

(iv) *Velocity profile inside the neck*

To link the behaviours inside and outside the cavity, we have to analyse the behaviour in the neck. To do so, we use (B8a,b) in (B3) along with (B9a,b). At the dominant orders we have

$$\partial_{x_\mu}\phi_\mu^0 = \partial_{x_\mu}\phi_\mu^1 = 0, \quad \text{hence } \phi_\mu^0(z_m, t),\ \phi_\mu^1(z_m, t). \tag{B43}$$

We also have that

$$\partial_{x_\mu} u_\mu^{-1} = \partial_{x_\mu} u_\mu^0 = 0, \quad \text{hence } u_\mu^{-1} = u_\mu^0 = 0, \tag{B44}$$

because of the Neumann boundary conditions at $x_\mu = 0, \ell_\mu$. At the next order, we have $v_\mu^{-1} = \partial_{x_\mu}\phi_\mu^0$ from which we deduce that v_μ^{-1} does not depend on x_μ. We also have $\partial_{z_m} v_\mu^{-1} + \partial_{x_\mu} u_\mu^1 = 0$, that we integrate to get $\partial_{z_m} v_\mu^{-1} = \partial_{z_m z_m}\phi_\mu^0 = 0$ (the velocity is constant and the potential is linear in the neck). Making use of the matching conditions (B17) results in

$$\phi_\mu^0(-h_m^+, t) = \check{\phi}_\mu^0(t) = \check{\phi}_m^0(t), \quad \phi_\mu^0(-(h_m^+ + e_m), t) = \hat{\phi}_\mu^0(t) = \hat{\phi}_m^0(t) = \phi^0(0, t). \tag{B45a,b}$$

Since ϕ_μ^0 is a linear function of z_m, we deduce that

$$\phi_\mu^0(z_m, t) = \frac{\check{\phi}_m^0(t) - \phi^0(0, t)}{e_m}(z_m + h_m^+) + \check{\phi}_m^0(t), \quad v_\mu^{-1}(t) = \frac{\check{\phi}_m^0(t) - \phi^0(0, t)}{e_m}. \tag{B46a,b}$$

Now, in virtue of (B42) and the matching condition (B17) between the velocities in the neck and at its top end, we find that $\int_0^{\ell_\mu} v_\mu^{-1}(t)\,\mathrm{d}x_\mu = \pi\check{A}$, which simplifies given (B37a,b) and (B46a,b) to

$$\partial_{tt}\check{\phi}_m^0(t) + \frac{\ell_\mu}{e_m L_{o,m}}\check{\phi}_m^0(t) = \frac{\ell_\mu}{e_m L_{o,m}}\phi^0(0, t). \tag{B47}$$

Similarly, using (B42) and the matching condition (B17) between the velocities in the neck and its bottom end, we get that $\int_0^{\ell_\mu} v_\mu^{-1}(t)\,\mathrm{d}x_\mu = -\pi\hat{A}$, which given (B46$a$,$b$) simplifies to

$$\pi\hat{A} = \frac{\ell_\mu}{e_m}(\phi^0(0) - \check{\phi}_m^0) = L_{o,m}\partial_{tt}\check{\phi}_m^0(t). \tag{B48}$$

Coming back to (B31) we finally obtain the jump conditions on the velocity at order 1

$$[\![u^1]\!]_0 = -L_m\partial_x u^0(0, t) + L_{o,m}\partial_{tt}\check{\phi}_m^0(t). \tag{B49}$$

B.6. *Final non-dimensional effective problem*

The final effective problem is obtained by reconstructing a unique problem from the jump conditions (B20*a*,*b*)–(B23) at order 0 and (B28)–(B49) at order 1 as well as the shallow water equation (B18*a*–*c*). This unique problem is formulated across an enlarged interface which accounts for the finite thickness of the resonator (and which has vanished in the asymptotic analysis). We introduce the following potential and velocity fields

$$\phi(x,t)=\phi^0(x,t)+\varepsilon\phi^1(x,t),\quad u(x,t)=u^0(x,t)+\varepsilon u^1(x,t). \tag{B50a,b}$$

Outside the region of the resonant dock delimited by $x\in(0,kL)$, we have

$$\partial_x u-\partial_{tt}\phi=0,\quad u=\partial_x\phi, \tag{B51a,b}$$

which is the non-dimensional form of the shallow water equation in (2.3). The region of the resonant obstacle is replaced by jump conditions on the potential and velocity fields written between $x=0$ and $x=kL$. For that sake, we introduce $[\![f]\!]=f(kL)-f(0)$ and $\bar{f}=(f(kL)+f(0))/2$ with $kL=O(\varepsilon)$. The Taylor expansions of ϕ^0 and u^0 at $x=kL$ read

$$\phi^0(kL,t)=\phi^0(0^+,t)+kL\frac{\partial\phi^0}{\partial x}(kL,t),\quad u^0(kL,t)=u^0(0^+)+kL\frac{\partial u^0}{\partial x}(kL,t), \tag{B52a,b}$$

up to $O(\varepsilon^2)$. Gathering the jump conditions (B20*a*,*b*) and (B28) on the potential and (B23) and (B49) for the velocity, we finally obtain

$$[\![\phi]\!]=kH\mathcal{B}\,\overline{\partial_x\phi},\quad [\![u]\!]=kL_o\partial_{tt}\check{\phi}(t), \tag{B53a,b}$$

which is the non-dimensional form of the transmission conditions in (2.3). The time-dependent function $\check{\phi}$ is the uniform potential inside the cavity which satisfies an oscillator equation driven by the average value of the potential outside the cavity. From (B47), with $\ell_\mu=g\ell/\omega^2H^2$ and $(e_m,L_{o,m})=(e/H,L_o/H)$, it takes the form (equivalent up to $O(\varepsilon)$)

$$\omega^2\partial_{tt}\check{\phi}(t)+\frac{g\ell}{eL_o}\check{\phi}(t)=\frac{g\ell}{eL_o}\bar{\phi}(t), \tag{B54}$$

which is the non-dimensional form of (2.11) along with (2.10).

Appendix C. Multimodal method

The multimodal method uses matchings of the solution written in the seven domains shown in figure 13. The procedure is classic and we give here the main steps that we have used. In each domain, the solution is expanded on a basis of transverse functions (along z) which satisfy exactly two boundary conditions, the dynamical condition at the free surface at $z=0$ (regions 1, 3, 4, 6 and 7) and Neumann boundary condition on rigid parts at $z=-h^+$ (regions 3 and 6), $z=-H+h^-$ (regions 2 and 5), $z=-H$ (regions 1, 2, 4, 5 and 7). Specifically we consider the following expansions

$$\left\{\begin{aligned}
\varphi^{(1)}(x,z) &= \mathrm{e}^{\mathrm{i}K_1x}\phi_1(z) + \sum_{n=1}^{N} R_n\mathrm{e}^{-\mathrm{i}K_nx}\phi_n(z),\\
\varphi^{(2)}(x,z) &= \sum_{n=1}^{N^-}\left(A_n^+\mathrm{e}^{-a_nx} + A_n^-\mathrm{e}^{a_n(x-x_2)}\right)\psi_n(z) + A_0x + a_0,\\
\varphi^{(3)}(x,z) &= \sum_{n=1}^{N^+} B_n\frac{\cos k_n(x-x_1)}{\cos k_n(x_2-x_1)}\varphi_n(z),\\
\varphi^{(4)}(x,z) &= \sum_{n=1}^{N}\left(C_n^+\mathrm{e}^{\mathrm{i}K_n(x-x_2)} + C_n^-\mathrm{e}^{-\mathrm{i}K_n(x-x_3)}\right)\phi_n(z),\\
\varphi^{(5)}(x,z) &= \sum_{n=1}^{N^-}\left(D_n^+\mathrm{e}^{-a_n(x-x_3)} + D_n^-\mathrm{e}^{a_n(x-x_4)}\right)\psi_n(z) + D_0(x-x_3) + d_0,\\
\varphi^{(6)}(x,z) &= \sum_{n=1}^{N^+} E_n\frac{\cos k_n(x-x_4)}{\cos k_n(x_4-x_3)}\varphi_n(z),\\
\varphi^{(7)}(x,z) &= \sum_{n=1}^{N} T_n\mathrm{e}^{\mathrm{i}K_n(x-L)}\phi_n(z).
\end{aligned}\right. \tag{C1}$$

In the above expansions, the series are truncated as is done in the numerics. The (k_n, K_n) are the roots of the dispersion relation $\omega^2 = gk\tanh kh$ for (h^+, H) (with (k_1, K_1) the real roots and $(k_n, K_n)_{n>1}$ the imaginary roots) and $a_n = n\pi/h^-$. The set of transverse eigenfunctions are

$$\left\{\begin{aligned}
&\phi_n(z) = N_n\cosh(K_n(z+H)), && N_n = \sqrt{\frac{\sinh(2K_nH)}{4K_n} + \frac{H}{2}},\\
&\varphi_n(z) = n_n\cosh(k_n(z+h^+)), && n_n = \sqrt{\frac{\sinh(2k_nh^+)}{4k_n} + \frac{h^+}{2}},\\
&\psi_n(z) = \sqrt{\frac{2}{h^-}}\cos(a_n(z+H-h^-)),
\end{aligned}\right. \tag{C2}$$

which are orthogonal and normalized considering the scalar products

$$(f,g) = \int_{-H}^{0} f(z)g(z)\,\mathrm{d}z, \quad (f,g)^+ = \int_{-h^+}^{0} f(z)g(z)\,\mathrm{d}z,$$
$$(f,g)^- = \int_{-H}^{-H+h^-} f(z)g(z)\,\mathrm{d}z, \tag{C3a–c}$$

namely, we have $(\phi_n, \phi_m) = \delta_{mn}$, $(\varphi_n, \varphi_m)^+ = \delta_{mn}$ and $(\psi_n, \psi_m)^- = \delta_{mn}$. The solution is obtained by matching the potentials and their derivatives $u = \partial_x\varphi$ at the junction between two regions. These matchings read:

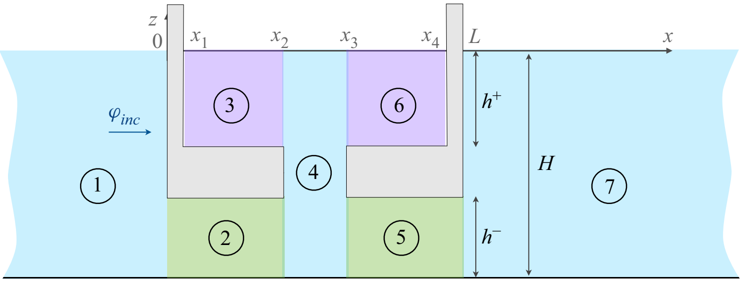

Figure 13. The seven domains used in the multimodal method.

Matchings at $x = 0$

$$\left.\begin{aligned} &m = 1, \ldots N^-, \quad (\varphi^{(1)}_{|x=0}, \psi_m)^- = (\varphi^{(2)}_{|x=0}, \psi_m)^-, \quad (\varphi^{(1)}_{|x=0}, 1)^- = (\varphi^{(2)}_{|x=0}, 1)^-, \\ &m = 1, \ldots N, \quad (u^{(1)}_{|x=0}, \phi_m) = (u^{(2)}_{|x=0}, \phi_m)^-. \end{aligned}\right\} \tag{C4}$$

Matchings at $x = x_2$

$$\left.\begin{aligned} &m = 1, \ldots N^-, \quad (\varphi^{(2)}_{|x_2}, \psi_m)^- = (\varphi^{(4)}_{|x_2}, \psi_m)^-, \quad (\varphi^{(2)}_{|x_2}, 1)^- = (\varphi^{(4)}_{|x_2}, 1)^-, \\ &m = 1, \ldots N^+, \quad (\varphi^{(3)}_{|x_2}, \varphi_m)^+ = (\varphi^{(4)}_{|x_2}, \varphi_m)^+, \\ &m = 1, \ldots N, \quad (u^{(2)}_{|x_2}, \phi_m)^- + (u^{(3)}_{|x_2}, \phi_m)^+ = (u^{(4)}_{|x_2}, \phi_m). \end{aligned}\right\} \tag{C5}$$

Matchings at $x = x_3$

$$\left.\begin{aligned} &m = 1, \ldots N^-, \quad (\varphi^{(4)}_{|x_3}, \psi_m)^- = (\varphi^{(5)}_{|x_3}, \psi_m)^-, \quad (\varphi^{(4)}_{|x_3}, 1)^- = (\varphi^{(5)}_{|x_3}, 1)^-, \\ &m = 1, \ldots N^+, \quad (\varphi^{(4)}_{|x_3}, \varphi_m)^+ = (\varphi^{(6)}_{|x_3}, \varphi_m)^+, \\ &m = 1, \ldots N, \quad (u^{(4)}_{|x_3}, \phi_m) = (u^{(5)}_{|x_3}, \phi_m)^- + (u^{(6)}_{|x_3}, \phi_m)^+. \end{aligned}\right\} \tag{C6}$$

Matchings at $x = L$

$$\left.\begin{aligned} &m = 1, \ldots N^-, \quad (\varphi^{(5)}_{|L}, \psi_m)^- = (\varphi^{(7)}_{|x=0}, \psi_m)^-, \quad (\varphi^{(5)}_{|L}, 1)^- = (\varphi^{(7)}_{|L}, 1)^-, \\ &m = 1, \ldots N, \quad (u^{(5)}_{|L}, \phi_m)^- = (u^{(7)}_{|L}, \phi_m). \end{aligned}\right\} \tag{C7}$$

These matchings provide $(4N + 2N^+ + 4N^- + 4)$ relations needed to solve the system which is set on the $(4N + 2N^+ + 4N^- + 4)$ unknown coefficients: $\boldsymbol{R}, \boldsymbol{C}^{\pm}, \boldsymbol{T}$ $(4N)$, $\boldsymbol{A}^{\pm}, A_0, a_0, \boldsymbol{D}^{\pm}, D_0, d_0$ $(4N^- + 4)$ and $\boldsymbol{B}, \boldsymbol{E}$ $(2N^+)$, where $\boldsymbol{R}$ is the column vector with $(R_n)_{n=1,\ldots,N}$ components (the same for the other vectors). They imply two matrices $\boldsymbol{M}^{\pm}$ and a column vector $\boldsymbol{V}$ whose components are

$$\boldsymbol{M}^-_{mn} = (\psi_m, \phi_n)^-, \quad \boldsymbol{M}^+_{mn} = (\varphi_m, \phi_n)^+, \quad V_m = (\phi_m, 1)^-. \tag{C8a–c}$$

The matchings can be written in a matrix form

$$\left\{\begin{array}{ll}
\boldsymbol{M}^{-}R-\left(A^{+}+\boldsymbol{e}_{a}A^{-}\right)=s_{1}, & {}^{t}VR-h^{-}a_{0}=s_{0},\\
\mathrm{i}\boldsymbol{K}R-\boldsymbol{a}\,{}^{t}\boldsymbol{M}^{-}\left(A^{+}-\boldsymbol{e}_{a}A^{-}\right)+VA_{0}=s_{3}, & \\
 & \\
\left(\boldsymbol{e}_{a}A^{+}+A^{-}\right)-\boldsymbol{M}^{-}\left(C^{+}+\boldsymbol{e}_{K}C^{-}\right)=\boldsymbol{0}, & h^{-}\left(x_{2}A_{0}+a_{0}\right)-{}^{t}V\left(C^{+}+\boldsymbol{e}_{K}C^{-}\right)=0,\\
-B+\boldsymbol{M}^{+}\left(C^{+}+\boldsymbol{e}_{K}C^{-}\right)=\boldsymbol{0}, & \\
\boldsymbol{a}\,{}^{t}\boldsymbol{M}^{-}\left(\boldsymbol{e}_{a}A^{+}-A^{-}\right)-VA_{0}+\boldsymbol{T}_{k}\,{}^{t}\boldsymbol{M}^{+}B & +\mathrm{i}\boldsymbol{K}\left(C^{+}-\boldsymbol{e}_{K}C^{-}\right)=0,\\
 & \\
\boldsymbol{M}^{-}\left(\boldsymbol{e}_{K}C^{+}+C^{-}\right)-\left(D^{+}+\boldsymbol{e}_{a}D^{-}\right)=0, & {}^{t}(\boldsymbol{e}_{K}V)C^{+}+{}^{t}VC^{-}-h^{-}d_{0}=0,\\
\boldsymbol{M}^{+}\left(\boldsymbol{e}_{K}C^{+}+C^{-}\right)-E=\boldsymbol{0}, & \\
\mathrm{i}\boldsymbol{K}\left(\boldsymbol{e}_{K}C^{+}-C^{-}\right)+\boldsymbol{a}\,{}^{t}\boldsymbol{M}^{-}\left(D^{+}-\boldsymbol{e}_{a}D^{-}\right) & -VD_{0}-\boldsymbol{T}_{k}\,{}^{t}\boldsymbol{M}^{+}E=\boldsymbol{0},\\
 & \\
\boldsymbol{e}_{a}D^{+}+D^{-}-\boldsymbol{M}^{-}T=\boldsymbol{0}, & {}^{t}VT-h^{-}x_{2}D_{0}-d_{0}=0,\\
\boldsymbol{a}\,{}^{t}\boldsymbol{M}^{-}\left(\boldsymbol{e}_{a}D^{+}-D^{-}\right)-VD_{0}+\mathrm{i}\boldsymbol{K}T=\boldsymbol{0}, &
\end{array}\right. \tag{C9}$$

where $\boldsymbol{a}=\mathrm{diag}(a_n)$, $\boldsymbol{e}_a=\mathrm{diag}(\mathrm{e}^{-a_n x_2})$, $\boldsymbol{K}=\mathrm{diag}(K_n)$, $\boldsymbol{e}_K=\mathrm{diag}(\mathrm{e}^{\mathrm{i}K_n(x_3-x_2)})$ and $\boldsymbol{T}_k=\mathrm{diag}(k_n\tan(k_n(x_2-x_1)))$ are diagonal matrices and where the source terms read $s_{1,m}=-M_{m1}$, $s_0=-V_1$ and $s_{3,m}=-iK_1\delta_{m1}$. The above system can be then inverted which provide the solution in each domain, and the scattering coefficients.

REFERENCES

ARCHER, A.J., WOLGAMOT, H.A., ORSZAGHOVA, J., BENNETTS, L.G., PETER, M.A. & CRASTER, R.V. 2020 Experimental realization of broadband control of water-wave-energy amplification in chirped arrays. *Phys. Rev. Fluids* **5** (6), 062801.

BARTHOLOMEUSZ, E.F. 1958 The reflexion of long waves at a step. *Proc. Camb. Phil. Soc.* **54** (1), 106–118.

BENNETTS, L.G., PETER, M.A. & CRASTER, R.V. 2018 Graded resonator arrays for spatial frequency separation and amplification of water waves. *J. Fluid Mech.* **854**, R4.

BENNETTS, L.G., PETER, M.A. & CRASTER, R.V. 2019 Low-frequency wave-energy amplification in graded two-dimensional resonator arrays. *Phil. Trans. R. Soc. Lond.* A **377** (2156), 20190104.

BOBINSKI, T., MAUREL, A., PETITJEANS, P. & PAGNEUX, V. 2018 Backscattering reduction for resonating obstacle in water-wave channel. *J. Fluid Mech.* **845**, R4.

CAFLISCH, R.E., MIKSIS, M.J., PAPANICOLAOU, G.C. & TING, L. 1985 Effective equations for wave propagation in bubbly liquids. *J. Fluid Mech.* **153**, 259–273.

D'ALEMBERT, J.L.R. 1747 Memoires de l'Academie royale des sciences et belles lettres. Classe de mathematique. (Paris), vol. 3, 214–219.

DUPONT, G., GUENNEAU, S., KIMMOUN, O., MOLIN, B. & ENOCH, S. 2016 Cloaking a vertical cylinder via homogenization in the mild-slope equation. *J. Fluid Mech.* **796**, R1.

DUPONT, G., REMY, F., KIMMOUN, O., MOLIN, B., GUENNEAU, S. & ENOCH, S. 2017 Type of dike using *c*-shaped vertical cylinders. *Phys. Rev.* B **96** (18), 180302.

EVANS, D.V. 1975 A note on the total reflexion or transmission of surface waves in the presence of parallel obstacles. *J. Fluid Mech.* **67** (3), 465–472.

EVANS, D.V. 1978 The oscillating water column wave-energy device. *IMA J. Appl. Maths* **22** (4), 423–433.

EVANS, D.V. & MORRIS, C.A.N. 1972 Complementary approximations to the solution of a problem in water waves. *IMA J. Appl. Maths* **10** (1), 1–9.

FARHAT, M., GUENNEAU, S., ALÙ, A. & WU, Y. 2020 Scattering cancellation technique for acoustic spinning objects. *Phys. Rev.* B **101** (17), 174111.

HELMHOLTZ, H. & ELLIS, A.J. 1954 *On the Sensations of Tone as a Physiological Basis for the Theory of Music*. Dover.

IIDA, T. & KASHIWAGI, M. 2018 Small water channel network for designing wave fields in shallow water. *J. Fluid Mech.* **849**, 90–110.

INGARD, U. 1953 On the theory and design of acoustic resonators. *J. Acoust. Soc. Am.* **25** (6), 1037–1061.

ISAACS, J.D. & WIEGEL, R.L. 1949 The measurement of wave heights by means of a float in an open-end pipe. *EOS Trans. AGU* **30** (4), 501–506.

JIMÉNEZ, N., ROMERO-GARCÍA, V., PAGNEUX, V. & GROBY, J.-P. 2017 Rainbow-trapping absorbers: broadband, perfect and asymmetric sound absorption by subwavelength panels for transmission problems. *Sci. Rep.* **7** (1), 13595.

LINTON, C.M. 2011 Water waves over arrays of horizontal cylinders: band gaps and Bragg resonance. *J. Fluid Mech.* **670**, 504–526.

LINTON, C.M. & EVANS, D.V. 1990 Compressed air breakwater. In *Proceedings of the 5th International Workshop on Water Waves and Floating Bodies, Manchester, UK*, pp. 109–113.

MAKWANA, M.P., LAFORGE, N., CRASTER, R.V., DUPONT, G., GUENNEAU, S., LAUDE, V. & KADIC, M. 2020 Experimental observations of topologically guided water waves within non-hexagonal structures. *Appl. Phys. Lett.* **116** (13), 131603.

MAUREL, A., MARIGO, J.-J., COBELLI, P., PETITJEANS, P. & PAGNEUX, V. 2017 Revisiting the anisotropy of metamaterials for water waves. *Phys. Rev.* B **96** (13), 134310.

MAUREL, A., PHAM, K. & MARIGO, J.-J. 2019 Scattering of gravity waves by a periodically structured ridge of finite extent. *J. Fluid Mech.* **871**, 350–376.

MEI, C.C., STIASSNIE, M. & YUE, D. 1989 *Theory and Applications of Ocean Surface Waves: Part 1: Linear Aspects Part 2: Nonlinear Aspects*. World Scientific.

MEI, C.C., STIASSNIE, M. & YUE, D.K.-P. 2005 *Theory and Applications of Ocean Surface Waves: Nonlinear Aspects*, vol. 2. World Scientific.

MERCIER, J.-F., MARIGO, J.-J. & MAUREL, A. 2017 Influence of the neck shape for Helmholtz resonators. *J. Acoust. Soc. Am.* **142** (6), 3703–3714.

MOLIN, B. 2001 On the piston and sloshing modes in moonpools. *J. Fluid Mech.* **430**, 27–50.

MOLIN, B., ZHANG, X., HUANG, H. & REMY, F. 2018 On natural modes in moonpools and gaps in finite depth. *J. Fluid Mech.* **840**, 530–554.

MONSALVE, E., MAUREL, A., PETITJEANS, P. & PAGNEUX, V. 2019 Perfect absorption of water waves by linear or nonlinear critical coupling. *Appl. Phys. Lett.* **114** (1), 013901.

NEWMAN, J.N. 1974 Interaction of water waves with two closely spaced vertical obstacles. *J. Fluid Mech.* **66** (1), 97–106.

NEWMAN, J.N. 2014 Cloaking a circular cylinder in water waves. *Eur. J. Mech.* (B*/Fluids)* **47**, 145–150.

PARSONS, N.F. & MARTIN, P.A. 1994 Scattering of water waves by submerged curved plates and by surface-piercing flat plates. *Appl. Ocean Res.* **16** (3), 129–139.

PHAM, K., MERCIER, J.-F., FUSTER, D., MARIGO, J.-J. & MAUREL, A. 2020 Scattering of acoustic waves by a nonlinear resonant bubbly screen. *J. Fluid Mech.* **906**, A19.

PORTER, R. 2018 Cloaking in water waves. In *Handbook of Metamaterials and Plasmonics* (ed. S.A. Maier), vol. 2. World Scientific.

PORTER, R. 2019 An extended linear shallow-water equation. *J. Fluid Mech.* **876**, 413–427.

PORTER, R. & PORTER, D. 2003 Scattered and free waves over periodic beds. *J. Fluid Mech.* **483**, 129–163.

RAVINTHRAKUMAR, S., KRISTIANSEN, T., MOLIN, B. & OMMANI, B. 2019 A two-dimensional numerical and experimental study of piston and sloshing resonance in moonpools with recess. *J. Fluid Mech.* **877**, 142–166.

ROMERO-GARCÍA, V., JIMENEZ, N., THEOCHARIS, G., ACHILLEOS, V., MERKEL, A., RICHOUX, O., TOURNAT, V., GROBY, J.-P. & PAGNEUX, V. 2020 Design of acoustic metamaterials made of Helmholtz resonators for perfect absorption by using the complex frequency plane. *C. R. Phys.* **21** (7–8), 713–749.

TUCK, E.O. 1975 Matching problems involving flow through small holes. In *Advances in Applied Mechanics* (ed. C.-S. Yih), vol. 15, pp. 89–158. Elsevier.

TUCK, E.O. 1977 Some classical water-wave problems in varying depth. In *Waves on Water of Variable Depth* (ed. D.G. Provis & R. Radok), vol. 64, pp. 9–20. Springer.

ZHAO, W., TAYLOR, P.H., WOLGAMOT, H.A., MOLIN, B. & TAYLOR, R.E. 2020 Group dynamics and wave resonances in a narrow gap: modes and reduced group velocity. *J. Fluid Mech.* **883**, A22.